DEFORMATION AND ITS EFFECT ON RECRYSTALLIZATION IN MAGNESIUM ALLOY AZ31

BY

SHENGLONG LIANG, B.ENG

A Thesis Submitted to the School of Graduate Studies in

Partial Fulfillment of the Requirements for the

Degree Master of Applied Science

McMaster University © Copyright by Shenglong Liang, July 2012

McMaster University MASTER OF APPLIED SCIENCE (2012)

(Material Science & Engineering) Hamilton, Ontario

TITLE: Deformation and Its Effect on Recrystallization in Magnesium Alloy AZ31

AUTHOR: Shenglong Liang, B.Eng.

SUPERVISOR: Dr. Hatem S. Zurob

NUMBER OF PAGES: xvi, 78

Abstract

Sheet specimens of alloy AZ31 were cross-rolled to equivalent strains of 0.05, 0.10, 0.30, 0.40, 0.56, and 0.77. The microstructure evolution was examined using a combination of optical metallography (OM), Electron Backscattered Diffraction (EBSD), Transmission Electron Microscopy (TEM) and X-ray diffraction (XRD). The results revealed significant activity of basal and non-basal slip as well as twinning. The twins were mainly of the contraction and double-twin (contraction-extension) types. In addition to the micron scale (1-5μm) twins observed on EBSD patterns, nano-scale twins were observed. The nano twins had a width of less than 0.20μm and existed either as individual/isolated twins or as twin-bundles that are several microns thick. The number of nano twin-bundles increased with increasing strain. Shear bands were also observed to form at high strains and eventually led to the failure of the sheet. As for the texture evolution, analysis of the pole figures shows an evident strengthening of the basal texture during the cross-rolling.

Specimens of Mg alloy AZ31 cold-rolled to equivalent strains of 0.10 and 0.30 were selected and annealed at 250^{o}C. The progress of recrystallization was followed using OM, EBSD and TEM with special emphasis on the nucleation of recrystallization. The distribution of recrystallization nuclei was very heterogeneous due to the heterogeneity of the as-deformed microstructure. Twin/grain-boundary and twin/twin intersections as well as twin interiors were the dominant recrystallization nucleation sites. Significant recovery was observed in the non-recrystallized regions and this limited the growth of the recrystallized grains.

Keywords: cross-rolling, twin-bundle, strain localization, texture evolution and recrystallization

Acknowledgements

Almost two years passed away silently, it is the right time to look back and then forward. During my last two years, I have experienced happiness, depression, anxiety and reborn. I felt happy when the polishing was good; I felt depressed when the outcome was away from my expectations; I always felt anxious when I was working on the annealing experiments since a furnace fire caught by me and I feel reborn when I have finally obtained many interesting results, at lease from my point of view and know how to play with life, at present and in the future. In getting those experiment results, many people have contributed much time and energy to me and then to the accomplishment of this master thesis. I deeply appreciate them from the very bottom of my heart.

First of all, I would like to thank my supervisor Dr. Hatem. S. Zurob. Hatem is a great supervisor and a very nice, generous person. I was always encouraged to conduct the experiments with my own ideas, which leads to our amazing findings in the deformation of Mg alloy AZ31. Even though hatem might not be a top researcher in this field, his intelligence and diligence as a researcher do surprise me and he is always eager to learn the new knowledge on crystallography and comes up with bunches of innovative ideas, considering all the possibilities on one issue. Under his supervision, I have learnt how to do research and how to work with others. Also, I have to mention that hatem always left

the time for me to rest when I felt uncomfortable and took away much work from me. I really have to thank him as a great person, a great researcher and a great supervisor.

Second, several people helped a lot on the experiments analysis. For Transmission Electron Microscopy (TEM) research, I would like to thank Dr. Xiang Wang, the research associate in our group. The interesting findings cannot be confirmed without Xiang's fantastic TEM work. Xiang is also a very nice gentleman and so helpful that he will be always there whenever I have questions or requests on the research. For Electron Backscattered Diffraction (EBSD) research, I would like to thank Dr. Chris Butcher and Dr. Florent Lefevre-Schlick. Dr. Chris Butcher is a very knowledgeable and kind person. I can always get the answer, or the reference at least, to my question each time from him. Besides Chris, Dr. Florent Lefevre-Schlick, or simply "flo", helped me on the preparation of the EBSD samples which haven't been conducted successfully before at McMaster. For the X-ray diffraction (XRD) research, I would like to thank Dr. Jim Britten in chemistry department. His several discussions and tutorials deeply impressed me and I have learnt much on the XRD analysis. Without these people, this master thesis cannot be accomplished.

Third, beyond the experiments, many other friends and colleagues also helped and pushed me to the final line, either solving my questions or discussing an English term.

The interactions might be subtle but are equally vital to the fulfillment of the thesis. Those people are Sean Crawford, Md Kashif Rehman, Michael Nemcko, Annor Flicia, Yunfei Bai, Stella Zhang, etc. Without these people, my life at McMaster would be much more difficult and boring. I may not be able to list the people who helped me indirectly, but I also appreciate their opinions or helps.

Finally, I, again, would like to thank all the people mentioned or not mentioned here and I would like to dedicate this thesis to all of them.

Table of Contents

List of Figures and Tables

Figures:

Tables:

List of all Abbreviations

OM: Optical Metallography

EBSD: Electron Backscattered Diffraction

TEM: Transmission Electron Microscopy

XRD: X-ray Diffraction

CRSS: Critically Resolved Shear Stress

Chapter 1: Literature Review

1.1 Magnesium and Its Alloys

1.1.1 Overview

Magnesium alloys have typically been used in the as-cast condition due to their low formability at low temperatures [1], which is related to their hexagonal close-packed (HCP) structure. Recently, however, research on wrought magnesium alloys has intensified as reflected by the number of scientific articles published per year of Mg alloy AZ31 in Fig. 1.1. The high strength-to-weight ratio of wrought Mg alloys has drawn the attention of numerous industries, all over the world, including the automotive, aerospace and naval industries. The density of magnesium is about 2/3 that of aluminum and 1/4 that of iron, which gives magnesium an outstanding potential as a structure material.

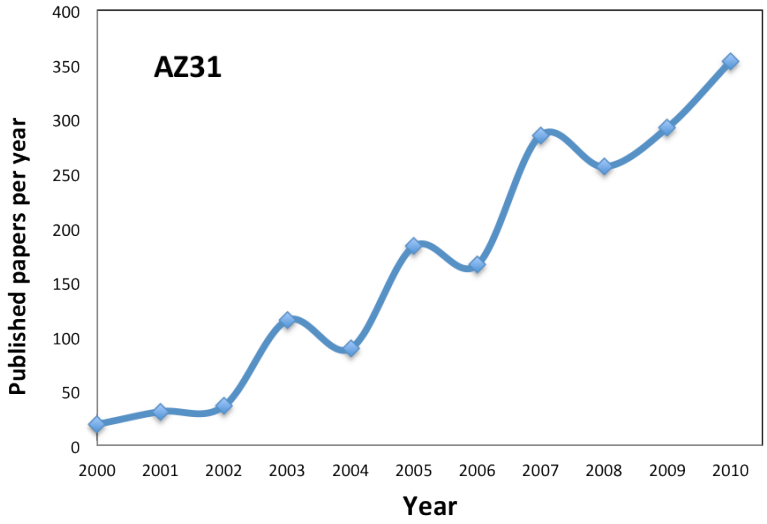

Fig. 1.1: Scientific articles on magnesium alloy AZ31 with respect to the year. Articles with AZ31 in subject/abstract/title were selected for comparison.

The B36 bomber aircraft may be taken as an example. The B36 uses 7500 lb of magnesium sheet and a further 2500 lb of castings, extrusions and forgings as part of the structure of the plane. A further 9000 lb of magnesium is used in auxiliary items, making 19,000 lb in total. Replacement of the magnesium by aluminum would have increased the overall weight of the bomber by as much as 4.5tons [2]. Therefore, such a weight reduction would improve performance and reduce emissions.

1.1.2 Mg Alloy AZ31

Magnesium alloy AZ31 is a member of the 'AZ' family of wrought alloys in which 'A' and 'Z' refer to Aluminum and Zinc, which are the main alloying additions. Alloy AZ31 is arguably the most widely available wrought Mg alloy; it nominally contains 3wt% Al and 1wt% Zn.

The ternary Mg-3%Al-1%Zn alloy has a one-phase microstructure under hot-working conditions; precipitation of the $Mg_{17}Al_{12}$ phase takes place below 200^{o}C. In practice, however, the presence of Mn in commercial AZ31 leads to the precipitation of various Al-Mn intermetallics as shown in Fig. 1.2 [3]. These particles provide strong pinning of grain-growth at high temperatures. In the context of the present work on recrystallization, it is essential to take into account the pinning effect of the particles.

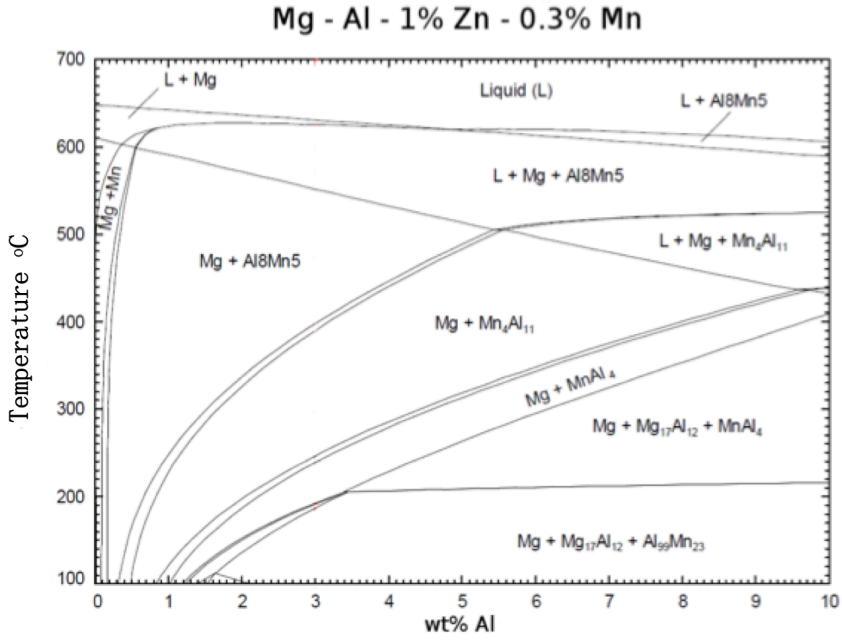

Fig. 1.2: Phase diagram of magnesium alloy AZ31 calculated by FactSAGE software with its light metal database [3].

1.2 Deformation

1.2.1 Slip

For HCP materials, the commonly observed slip systems are the basal, prismatic and pyramidal slip systems. In the case of magnesium, the main slip systems are the basal {0002}<11-20>, prismatic {10-10}<11-20>, pyramidal (type 1) {10-11}<11-20> and pyramidal (type 2) {11-22}<11-23> systems. They are drawn schematically in Fig. 1.3.

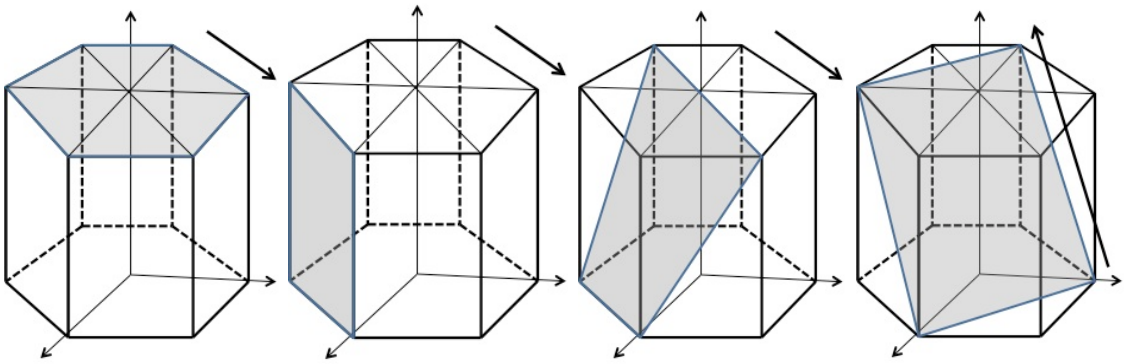

Fig. 1.3: Different slip systems in magnesium and its alloy. Basal slip, prismatic slip, pyramidal slip type 1 and pyramidal slip type 2 are drawn schematically in hcp crystals.

The CRSS plays an important role on the relative ease for dislocation gliding in different planes. Fig. 1.4 shows the CRSS for different slip systems as compiled by Hiura [4]. The absolute values may be debatable to some extent, but they could provide references of the magnitude of CRSS for different slip systems. From the CRSS data, we could notice that the predominant slip system in Mg alloy is the basal slip and extension twinning is first type of twining to be activated. The other slip systems are relatively much more difficult to operate with higher CRSS.

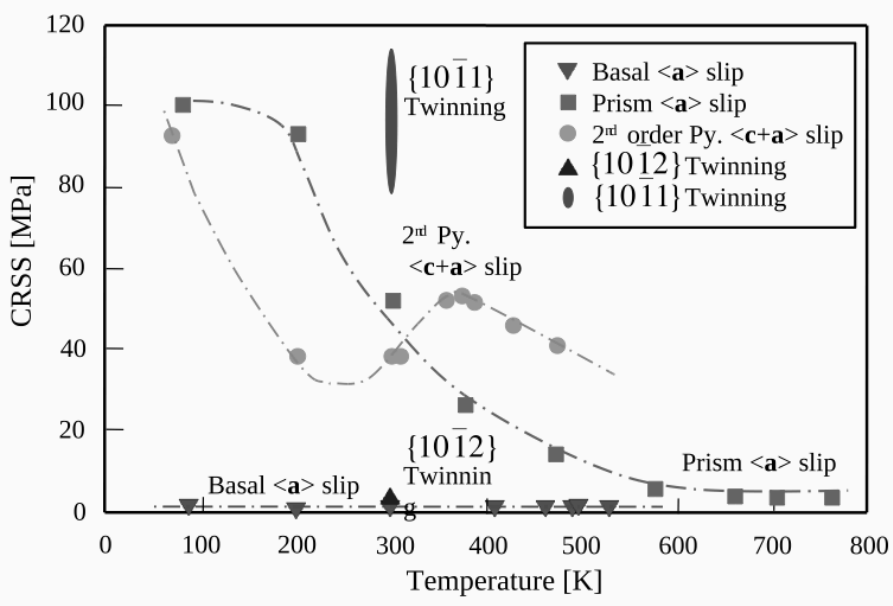

Fig. 1.4: CRSS plotted versus temperature showing the high correlation of temperature with the number of active slip systems in Mg [4].

From the theory of plasticity, five independent slip systems are needed to give an arbitrary shape change during deformation. For magnesium alloys[1], the <c+a> slip is relatively difficult to operate and only two active independent basal slip systems are available. Therefore, to accommodate the c-axis strain, deformation twinning is critical to the formability of Mg alloys.

[1] When discussing "magnesium alloys" in the thesis, we have excluded the Mg-RE (rare earth elements) alloys because in these alloys the <c+a> slip is more easily activated [14].

1.2.2 Twinning

Twins could be classified into mechanical and annealing twins. Mechanical twinning is very important for the deformation of Magnesium alloys because it can provide the needed c-axis strain component for generalized deformation [5]. To describe a twin, the twinning shear S, two undistorted planes, $K_1$and K_2, twinning shear direction $\eta_1$and the intersections η_2 of shear plane and K_2, are introduced as shown in Fig. 1.5. The shear strain S, can be calculated as:

$$S = 2cot2\varphi$$

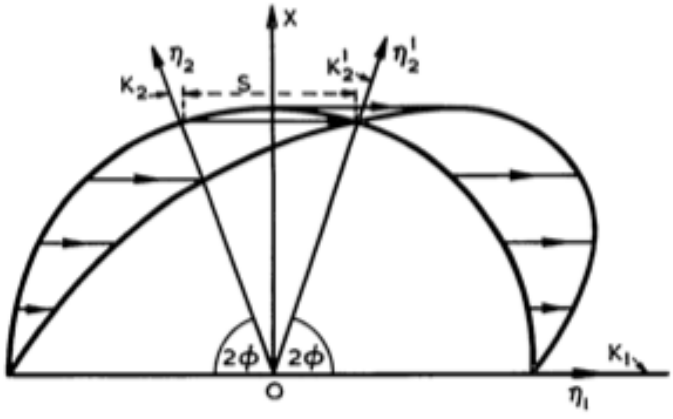

Fig. 1.5: Conversion of a sphere into an ellipsoid by the twinning shear η_1. Section is parallel to the plane of shear. S is the displacement at unit distance along OX [6].

The magnitude and sense of the shear vary with the c/a ratio of HCP materials and the shear plane on which the atoms are displaced. The movement that must be added to the twinning shear to describe the displacement of an atom to a position in the twinned crystal is usually termed a reshuffle [7]. For Magnesium alloys, the twinning elements could be summarized as followed in Table 1:

Table 1: The Twinning Elements for Magnesium Alloys [7].

	K_1	$\boldsymbol{\eta_1}$	K_2	$\boldsymbol{\eta_2}$	Magnitude of shear
Extension	10-12	-1011	10-12	10-1-1	-0.130
Contraction	10-11	10-12	-1013	30-32	0.137

It is of great importance to point out that the twinning type in Mg depends on the loading modes or the stress field. When the crystal is compressed perpendicular to the c-axis or pulled along the c-axis, the extension twin will occur to provide c-axis expansion strain. In contrast, compression along the c-axis and tension perpendicular to the c-axis would lead to contraction twins in order to provide c-axis contraction strain. That is why the sign of the shear for those two twins is different (Table 1). The third important type of twin is the second-order {10-11}-{10-12} twinning, i.e. the {10-12}

extension twins formed within the primary {10-11} contraction twins [8]. Another way to describe these three types of twins is in terms of the rotation angles around the <11-20> axis; extension twins <11-20>86.3°, contraction twins <11-20>56.2° and double twins <11-20>37.5°. The schematic twinning rotation relationships are shown in Fig. 1.6 [9].

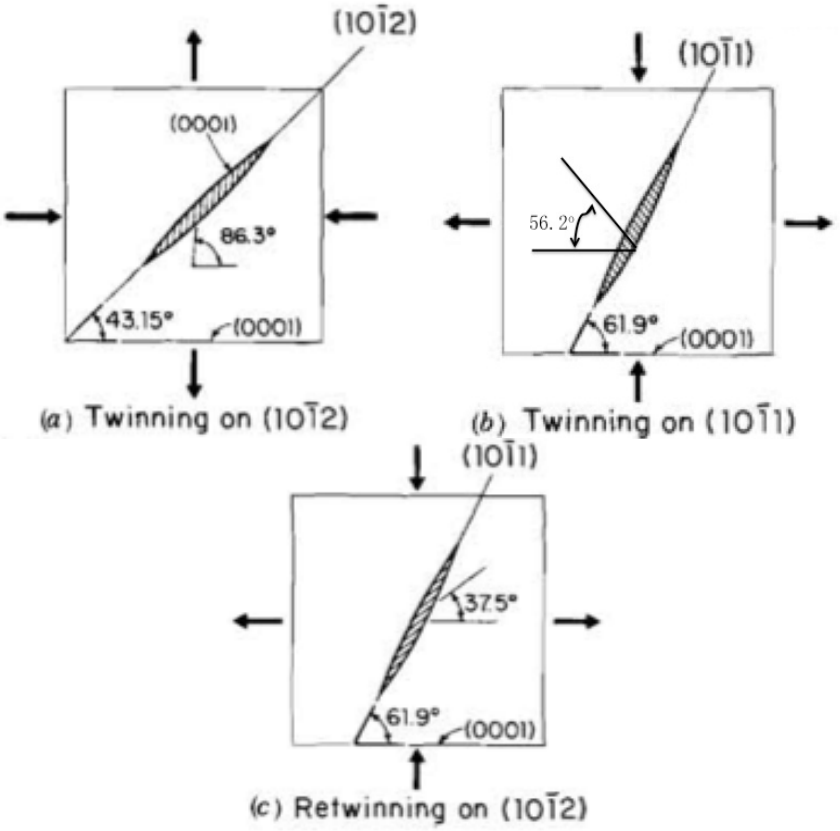

Fig. 1.6：Twinning on different planes and double twinning: (a) Twinning on {10-12}; (b) Twinning on {10-11} and (c) Retwinning on {10-12} [9].

1.2.3 Texture Evolution

The term “texture” refers to the preferred orientation of grains within the material. The development of preferred orientation would change the deformation behavior of the material. At the same time, it is well established that deformation can change the orientation of the lattice thus leading to the development of a certain texture. There is, therefore, an interplay between the role of deformation in creating the texture and the role of texture in facilitating deformation [7].

Basal<a> slip, prismatic<a> slip, pyramidal <a> slip and pyramidal <c+a> slip and {10-12}<10-11>extension twinning are the main deformation modes for HCP metals. The evolution of deformation texture in HCP metals and their alloys will develop in accordance with the relative contributions from the above four deformation paths (not including pyramidal <a> slip). Through these deformation processes, the slip plane will gradually rotate toward the rolling plane and the slip direction toward the rolling direction [10]. The variation of textures observed in hcp materials is related to the relative ease of slip and twinning, i.e. the relative critical resolved shear stresses, CRSS. In contrast to slip, where lattice rotations tend to proceed gradually with increasing deformation, twinning causes spontaneous, large-scale lattice rotations, even for low degrees of deformation [11].

Styczynski [12] had already examined the texture experimentally using X-ray Diffraction (XRD) and theoretically in terms of the viscoplastic Taylor model. Both

annealed and cold-rolled samples were examined with XRD in Fig. 1.7. From the results it can be concluded that the development of strong basal texture is a result of the microstructure evolution during deformation and not so dependent on the initial texture. To understand the associated mechanism, the Taylor model was introduced and four slip modes, namely, basal<a> slip, prismatic<a> slip, pyramidal <a> slip and pyramidal <c+a> slip and {10-12}<10-11>extension twinning were taken into account. Different combinations of these deformation modes were set up into the model and the results showed that a combination of basal <a>slip plus pyramidal <c+a>slip plus extension twinning (combination C in Ref [12]) led to very good agreement with experiment.

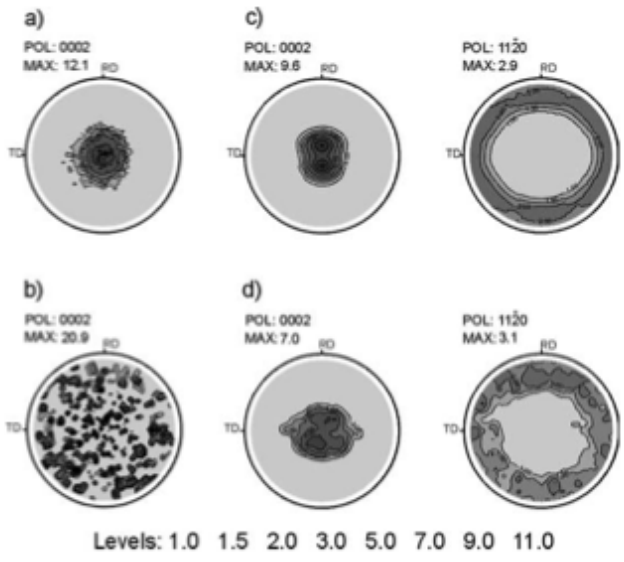

Fig. 1.7: Initial texture found in AZ31 (a) commercially recrystallized sheet and (b) squeeze-cast material. Texture after cold rolling of (c) commercially recrystallized sheet and (d) squeeze cast material [12].

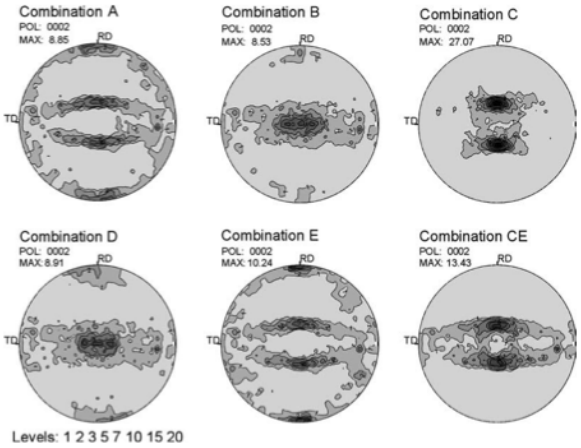

Designation	Slip and twinning combination	Relative CRSS
A	b + py1 + py2	1.0–1.0–3.0
B	b + py1 + tw	1.0–1.0–3.0
C	b + py2 + tw	1.0–3.0–0.5
D	b + pr + tw	1.0–1.5–3.0
E	b + pr + py2	1.0–1.0–3.0
CE	b + pr + py2 + tw	1.0–2.4–3.0–2.0

Fig. 1.8: Results of texture simulations for different combinations slip and twinning systems. For simplicity, “b” means basal slip; “py1” means pyramidal slip type 1; “py2” means pyramidal slip type 2 and “tw” means extension twinning. The relative CRSS was used in the model [12].

1.2.4 Shear Banding

Shear bands correspond to narrow regions of intense shear that occur independently of the grain structure and normal crystallographic considerations. In rolled materials, shear-bands occur at ~35^{o} to the rolling plane and parallel to the transverse direction. The formation of shear bands may change the deformation texture by rotating the material along the transverse direction and this may lead to changes in intensity of the texture [13].

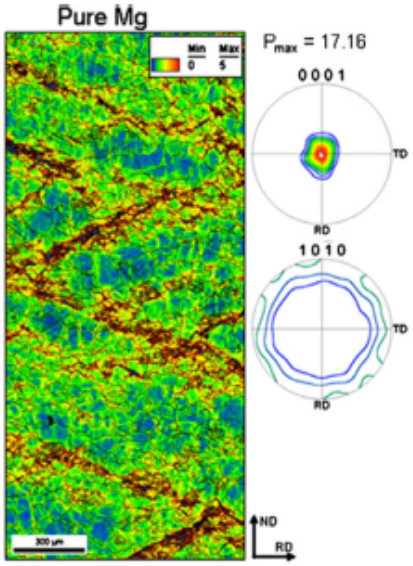

Fig. 1.9: Microstructure and texture of Mg sample after cold rolling up to 10% thickness reduction until the occurrence of first cracks. The microstructure is shown in terms of KAM[2] maps, the texture in the form of {0001} and {10-10} pole figures calculated from the EBSD maps [14].

In hcp magnesium alloys, the present study indicates that shear bands are not responsible for ductility improvement; on the contrary, they act as fracture initiation sites. As a consequence of the strong localization of strain in only a few shear bands in pure Mg, a critical strain is rapidly exceeded in the shear bands and crack formation starts early [14]. S. Sandlobes [14] found that in pure Mg strain is localized into narrow band-like structures. Other areas show only low internal misorientations (Fig. 1.9). This indicates strongly localized strain in only a few shear bands.

[2] KAM: Kernel average misorientation, calculated as the average over all misorientation angles determined between the centre and all edge pixels in a kernel of pixels in an orientation map. KAM values are applied as indicator of the internal strain [14].

Therefore, the formation of shear bands during deformation is of great importance to the formability of Mg alloys. One might not be able to prevent shear banding when deforming the material to relatively high strains, but one could delay the formation of shear bands by mutli-axial deformation [15, 16] which claims a much more homogeneous microstructure during deformation. In addition, the introduction of RE elements appears to reduce the intensity of shear bands and delay the onset of cracking [14].

1.3 Annealing

As the sample is deformed, large amount of point defects as well as dislocations are introduced leading to changes in material properties, such as yield strength or resistivity. Subsequent annealing is needed sometimes to restore the properties of the deformed materials back to their prior (non-deformed) values. Recovery and recrystallization are two main restoration or annealing processes.

1.3.1 Recovery

The term recovery refers to changes in a deformed material which partially restore the properties to their values before deformation. Dislocation recovery is not a single microstructural change but a series of events [13]. During annealing, the temperature is increased and dislocations become more mobile. When two dislocations of opposite sign meet then they effectively cancel out and their contribution to the stored energy is removed. After annihilation any remaining dislocations can align themselves into ordered arrays where their individual contribution to the stored energy is reduced by the overlapping of their strain fields. These processes can be described schematically in Fig. 1.10 [13].

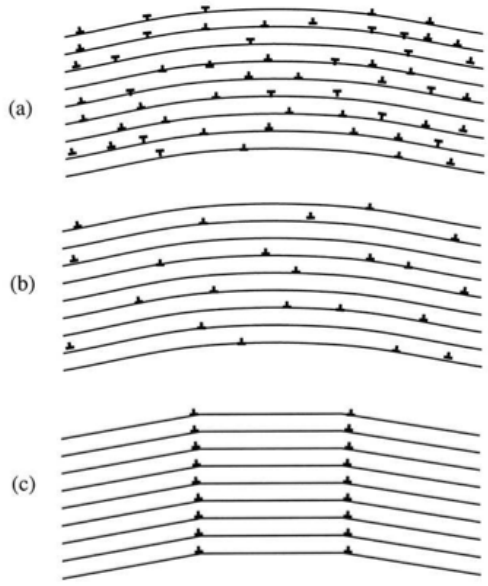

Fig. 1.10: Recovery by polygonization of a bent crystal containing edge dislocations: (a) As deformed, (b) After dislocation annihilation and (c) Formation of tilt boundaries [13].

Table 2: Stacking Fault Energy of Metals [17].

Metal	γ_{SFE} (mJm^{-2})	Metal	γ_{SFE} (mJm^{-2})
Aluminium	166	Zinc	140
Copper	78	Magnesium	125
Silver	22	91Cu:9Si	5
Gold	45	Zirconium	240
Nickel	128	304 Stainless steel	21
Cobalt (fcc)	15	70Cu:30Zn	20

Recovery and recrystallization compete for the stored energy in the material. At the same time, some recovery is believed to aid the "nucleation" of recrystallization by the growth of subgrains which could act as nuclei for recrystallization. Thus, understanding the effect of recovery on recrystallization is of great interest and importance. Besides the effect of strain and annealing temperature, the stacking fault energy is vital in determining the mechanism and kinetics of recovery. In metals of low stacking fault energy (Table 2) such as copper, alpha-brass and austenitic stainless steel, climb is difficult, and little recovery of the dislocation structure normally occurs prior to recrystallization. However, in metals of high stacking fault energy such as aluminium and alpha-iron, climb is rapid, and significant recovery may occur [13]. As can be seen in Table 2, magnesium has relatively high stacking fault energy suggesting rapid recovery kinetics in Mg. Attention should therefore be paid to the contribution of recovery to the softening of Mg and its alloys.

1.3.2 Recrystallization

Recrystallization involves the formation of new strain-free grains in certain parts of the specimen and the subsequent growth of these to consume the deformed or recovered microstructure [13]. Normally, recrystallization is divided into two stages; "nucleation" of the new strain-free grains and "growth" of the new grains into the deformed regions. One point to be clarified is that the word "nucleation" is not used in the classic thermodynamic sense, rather it simply refers to the formation of high angle grain boundaries that separate the growing low-dislocation density region from the deformed high dislocation density region.

To capture the recrystallization kinetics, the classical Kolmogorov, Johnson， Mehl and Avrami recrystallization model, simply called JMAK model, has typically been utilized. In its simplest form, the model employs a number of important assumptions:

1. Nuclei are randomly distributed in the material;
2. Nucleation rate, $\dot{N}$, is a constant through the recrystallization process;
3. Nuclei grow into the deformed material at a constant growth rate $\dot{G}$.

Under these assumptions, the extended recrystallized volume fraction, V_{EX}, is readily calculated. This quantity is defined as the recrystallized volume fraction in the absence of

any impingement effects and without taking account of the progressive consumption of the deformed material. It is simply calculated as:

$$V_{EX} = \int_0^t V\dot{N}dt' \quad \text{.....(1)}$$

where V, is the volume of nuclei formed from t' to t. This could be expressed as: $f\dot{G}^3(t-t')^3$,where f is the shape factor ($\frac{4\pi}{3}$ for the spheres). Thus:

$$V_{EX} = \int_0^t f\dot{G}^3(t-t')^3\dot{N}V_0dt' = \frac{f\dot{G}^3V_0t^4\dot{N}}{4} \quad \text{.....(2)}$$

During a time interval dt, the extended volume increases by dV_{EX}. As the untransformed fraction of material is 1-X_V (X_V=V/V_0), it follows that dV=(1-X_V)dV_{EX}.

$$V_{EX} = \int_0^{V_{EX}} dV_{EX} = \int_0^V \frac{dV}{1-\frac{V}{V_0}} = -V_0 \ln\left(1-\frac{V}{V_0}\right) \quad \text{.....(3)}$$

Then,

$$\frac{V}{V_0} = 1 - \exp\left(-\frac{V_{EX}}{V_0}\right) \quad \text{.....(4)}$$

$$X_V = 1 - \exp\left(-\frac{f\dot{N}\dot{G}^3t^4}{4}\right) \quad \text{.....(5)}$$

which is the commonly used expression for the recrystallized fraction as a function of time under the assumption of constant nucleation and growth rate. Another interesting limiting case is that of site saturated nucleation, in which the nuclei are assumed to be present at time t=0. In this case, the extended recrystallized volume fraction, V_{EX}, is given by:

$$V_{EX} = NV \quad \text{.....(6)}$$

where N is the total number of nucleation sites per unit volume at time t=0, and V is the volume of recrystallized grain, which is equal to $\frac{4\pi}{3}\dot{G}^3t^3$ for a spherical grain. Using the same derivation described above, the actual recrystallized fraction is found to be:

$$X_V = 1 - \exp\left(-\frac{4\pi N\dot{G}^3t^3}{3}\right) \quad \text{.....(7)}$$

In practice, the JMAK equation is commonly used in the generalized form:

$$X_V = 1 - \exp\left(-Bt^n\right) \quad \text{.....(8)}$$

$$\text{or } \ln\ln\{1/(1 - X_V)\} = \ln B + n\ln t \quad \text{.....(9)}$$

The Avrami exponent, n, is obtained from the slope of $\ln\ln\{1/(1 - X_V)\}$ vs. $\ln(t)$ plots. Experimentally, it is usually found that the Avrami exponent n varies from 1.5 to 3.4 for different strains at various temperatures in Fig. 1.11 [18].

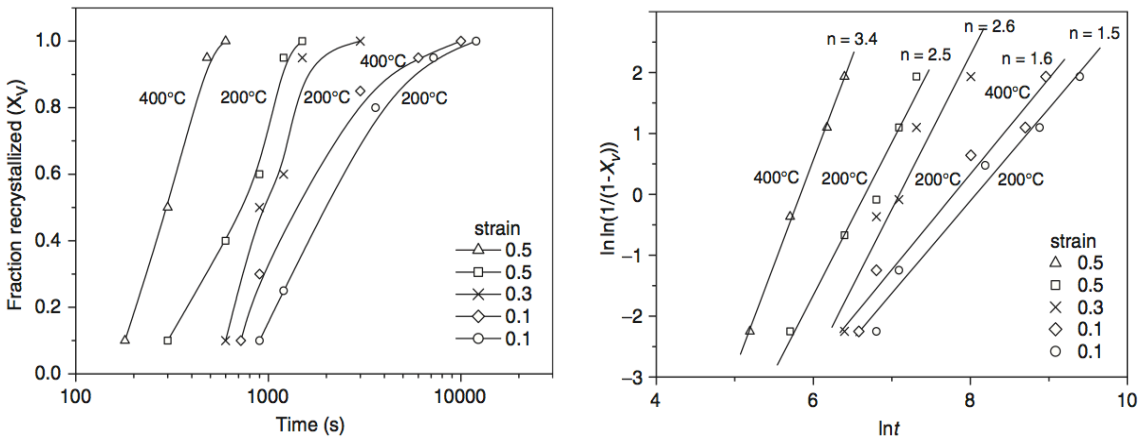

Fig. 1.11: Fraction recrystallized as a function of annealing time and recrystallization kinetics of AZ31 shown by JMAK plot for isothermal annealing [18].

Su et al [18] argued that the reason for the lower n might be the result of non-random recrystallization sites present in the deformed material. Another reason for the deviation of n is due to the growth rate of nuclei $\dot{G}$ not being a constant. Thus, the microstructure in the deformed states needs to be investigated in order to better understand the recrystallization behavior of magnesium alloy AZ31.

Static recrystallization of AZ31 was also investigated by Okrutny [3] who reported non-sigmoidal recrystallization kinetics under some conditions as shown in Fig. 1.12. These observations were modeled in terms of physically based model which assumed the existence of two regions with different stored-energy and misorientation gradients within the microstructure.

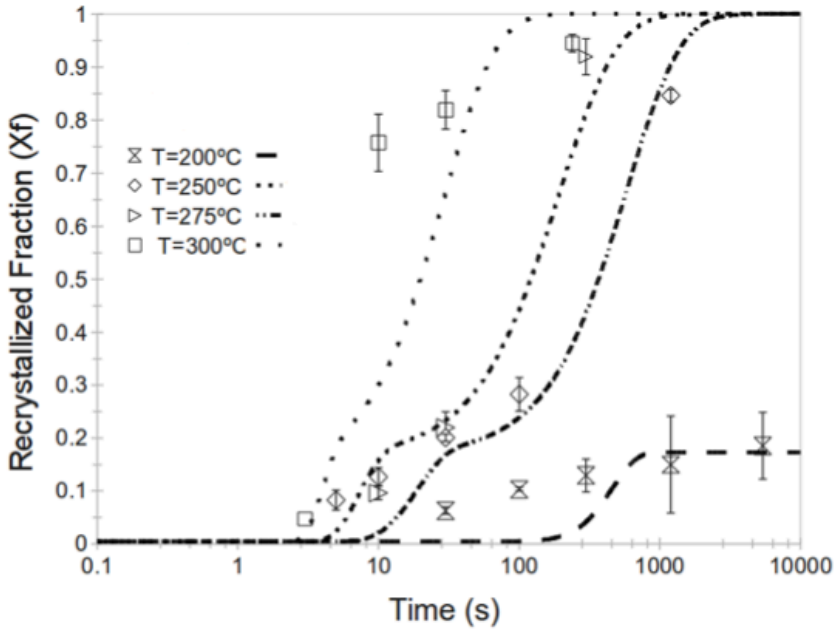

Fig. 1.12: Recrystallization data compared to modeling results [3].

Okrutny [3] argued that the initial increase in recrystallization volume fraction is due to recrystallization within the twins and correlated the initial recrystallized fraction (~20%) to the volume fraction of twins within the deformed specimen. The key weakness of the above model is that a number of parameters relating to the microstructure were used as fitting parameters. For example, it was assumed that a misorientation gradient of 4^{o}/um existed within the twins. Similarly, the mechanism for nucleation within the twins was presented with no experimental evidence or validation. One of the aims of this work, is therefore, to characterize the as-deformed state in order to quantify some of the key parameters that enter into models of recrystallization (e.g. orientation gradient, twin fraction and twin-types). In addition, the range of available recrystallization nucleation sites will be investigated with special emphasis on nucleation within twins and corresponding mechanism.

Chapter 2: Deformation Behavior of AZ31

2.1 Introduction

Magnesium alloys are attracting increasing attention for automotive applications due to their high-strength to weight ratio. The main limitation to widespread utilization of Mg alloys continues to be their poor formability at room temperature [19]. The c/a ratio of pure magnesium (hexagonal closed-packed) is 1.624 (ideal ratio~1.633) [20]. The origin of this limitation is often discussed in terms of the low number of operating independent slip systems in Mg at room temperature. Analysis of the Critical Resolved Shear Stress (CRSS) for slip in Mg reveals that basal slip {0001} <11-20> is the most favored slip system [21]. In addition, it is possible to have slips along on the <11-20> directions on the prismatic and pyramidal planes.

The above modes of deformation provide a total of 4 independent slip systems, with no possibility of accommodating deformation in the c-direction. Deformation along the c-direction could be accommodated by deformation twinning [22, 34] and possibly by slip on {11-22} <11-23> [23], which is often referred to as <c+a> slip. The extent to which <c+a> slip occurs has attracted a lot of attention because of the high CRSS for this kind of slip [21].

As for deformation twinning, the twins are generally divided into three groups: {10-12} <10-11> extension twinning (<11-20>86.3^{o}), {10-11} <10-12> contraction twinning (<11-20>56^{o}) and {10–11} {10-12} double twinning (<11-20>37.5^{o}) [8-9, 23-24, 29,33]. The first of these has a very low CRSS and is readily to be activated at low strains. As for contraction twinning, the CRSS is high and comparable to the CRSS for non-basal slip [4].

Recent studies have examined the microstructure evolution of AZ31 sheets during compression and cold rolling at room temperature [14, 25-28]. These results show a complex interaction of basal slip, twinning and shear-banding. The above studies, however, were limited to low strains because the onset of shear-banding and subsequent cracking precluded observations at high strains.

The present work will attempt to shed more light on the microstructure evolution of alloy AZ31 during cross-rolling through detailed examination of the deformed microstructure at multiple length scales. Special emphasis will be placed on the microstructure evolution at high strains, which could not be accessed using simple uniaxial deformation. Cross-rolling was used in order to access higher strains by delaying the development of severe strain localization. The present approach of changing the rolling direction in order to delay strain localization is similar to the multi-axial forging method used by [15] to deform AZ61 to very high strains.

2.2 Experimental

2.2.1 Sample Preparation

The experiments were carried on 2 mm thick sheets of alloy AZ31. The sheets were homogenized at 400^{o}C for 24 hrs to eliminate heterogeneities within the microstructure. In order to facilitate the observation of extensive twinning, the material was then subjected to grain-growth heat-treatment which consisted of small cold reduction of 5% followed by annealed at 470^{o}C for 2 hr.

The resulting grain-size was within 30~40μm, as shown in Fig. 2.1(a). The material was then cross-rolled at room-temperature to equivalent von Mises strains of 0.05, 0.10, 0.30, 0.40, 0.56, and 0.77. The rolling procedure consisted of a 0.03 mm reduction per pass and the rolling direction was rotated by 90^{o} after each pass. Cross-rolling was used in order to delay developments of shear-bands which lead to cracking failure in this material.

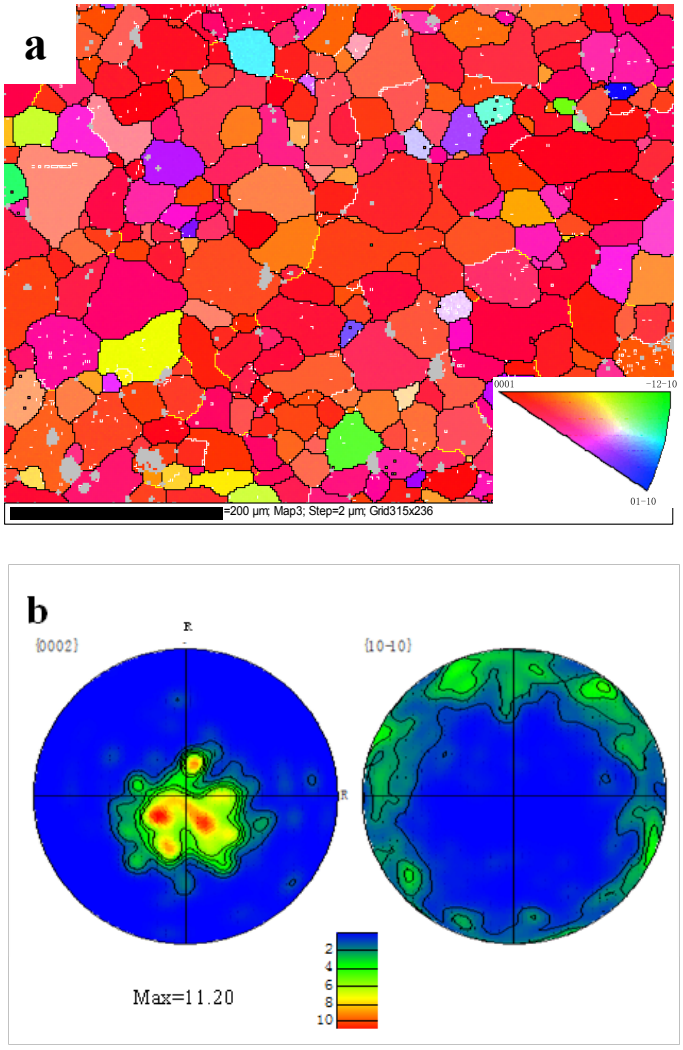

Fig. 2.1: As-annealed sample: (a) EBSD inverse pole figure (IPF) map showing orientation of each grain with respect to the crystal frame. The crystallographic < 0001> direction is perpendicular to the rolling plane and (b) {0002} and {10-10} pole figures showing an initial as-annealed texture.

2.2.2 Characterization

In order to obtain a complete description of the microstructure evolution, the material was characterized over a wide range of length scales; the samples were examined using Optical Microscopy (OM), Scanning Electron Microscopy (SEM), Transmission Electron Microscopy (TEM) and X-ray Diffraction (XRD).

The samples for optical metallography were prepared using standard metallographic methods followed by polishing with 9μm and 3μm diamond suspensions and 0.05μm colloidal silica solution (OPS). The grain boundaries were revealed using an etching solution of 6g picric, 100mL ethanol, 5mL acetic acid and 10mL water. Vickers microhardness measurements were performed on the as-polished specimens using a 50 g load. For each strain, 5 to 7 measurements were performed and the average and standard deviation were reported.

Electron Backscatter Diffraction (EBSD) observations were performed on the as-polished material using JEOL JSM-7000F FEG-SEM equipped with a CCD detector for EBSD analysis. An acceleration voltage of 20 keV and a working distance of 18.4 mm were used for the examination of sample microstructural development. The sample was tilted 70^{o} for the collection of data. Analysis of the EBSD results was performed using the HKL channel 5 software package.

TEM foils were prepared by twin-jet electro-polishing using a solution of 5.3 g lithium chloride, 11.16 g magnesium perchlorate, 500 ml methanol and 100 ml butyl cellosolve[3] at -50^{o}C and 50-90 V. Microstructure analysis was conducted using PHILIPS CM12 operating at 120KV.

Texture measurements were performed using a Bruker X-ray diffraction (XRD) goniometer. Texture analysis and the construction of pole figures were carried out with the aid of the popLA [35] and MTEX software packages [36].

It is worth pointing out that the OM and EBSD observations were carried out on the cross section while TEM observations were carried out in the plane of the sheet due to the difficulty in preparing foils in the cross-cross section direction. Similarly, the XRD measurements were taken from the plane of the sheet in order to obtain a better signal.

2.3 Results

2.3.1 Optical Microscopy

Optical microscopy was used to examine the global microstructure evolution. The microstructure evolution as a function of strain is shown in Fig. 2.2. Already at a strain of 0.05 twinning had occurred in some grains but most grains remained untwined.

[3] butyl cellosolve is the commercial name for Ethylene Glycol Monobutyl Ether, available from Dow Chemicals.

When the strain was increased to 0.10, twins could be observed in most grains. Further deformation resulted in a significant increase in the number of twins as seen in Fig. 2.2(c) and (d) corresponding to strains of 0.30 and 0.40. For high strains (> 0.30) individual twins became difficult to distinguish. Instead, one frequently observed bands similar to those shown in Fig. 2.3. These bands are actually bundles of finer twins as will be shown in subsequent sections. It is also interesting to note that many of the twins and/or bands present in the highly deformed samples were curved, which suggests that these twins were sheared by subsequent deformation.

Evidence of strain localization could be observed at a strain of 0.30 and becomes increasing more apparent at higher strains. At strains of 0.56 and 0.77 features resembling shear bands could be observed throughout the microstructure. In the present study, two sets of shear bands on each cross section were formed due to the cross-rolling procedure which was employed. The rolling plane normal (ND) and the cross rolling direction (CR) are shown in Fig. 2.2(f). The shear bands are approximately $\pm 35^{o}$ away from the rolling plane [13] and shear bands in Fig. 2.2(f) have similar angular relationships with the rolling plane.

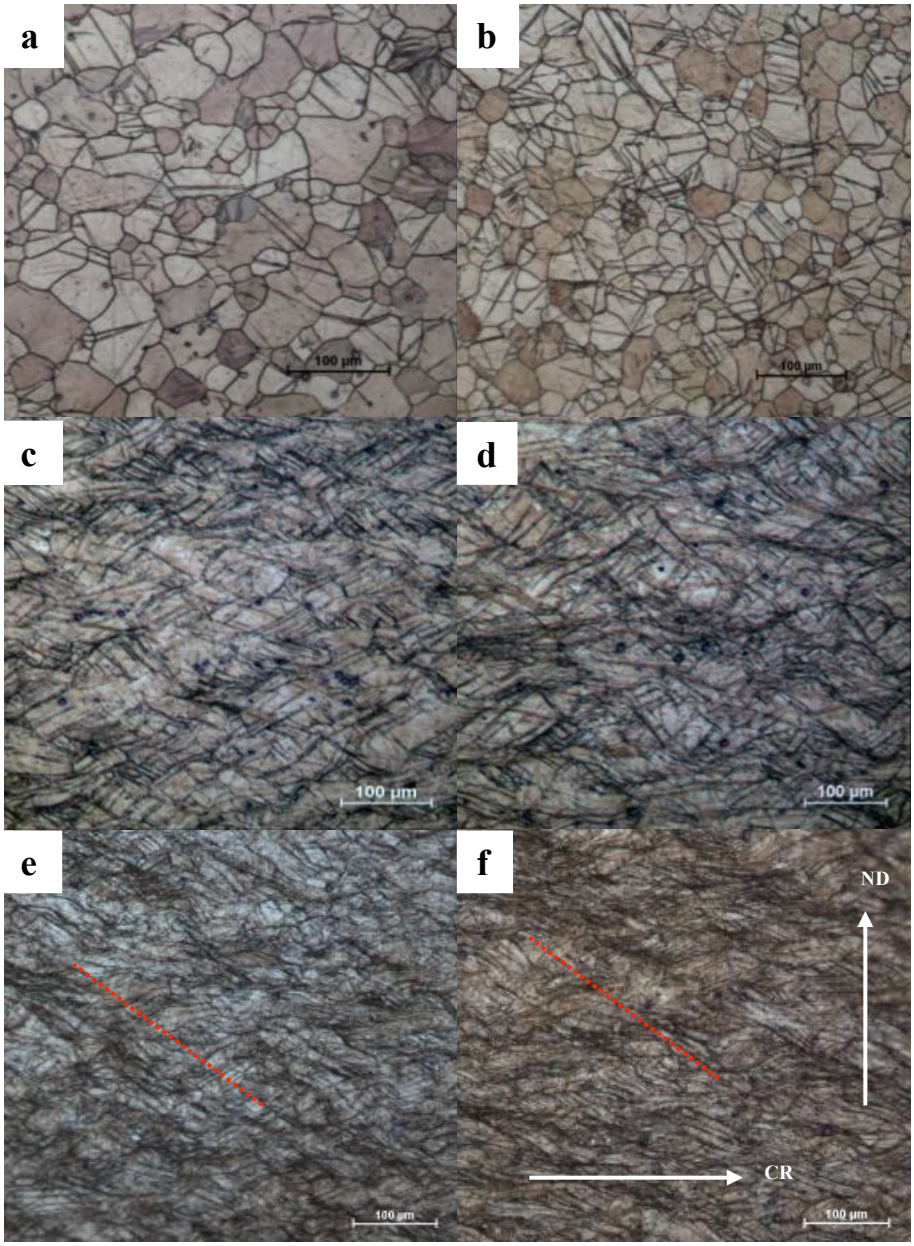

Fig. 2.2: Evolution of the microstructure as a function of deformation strains: (a) 0.05; (b) 0.10; (c) 0.30; (d) 0.40; (e) 0.56; (f) 0.77. The red dotted lines show the typical shear bands directions (about ±35^{o} from the rolling plane).

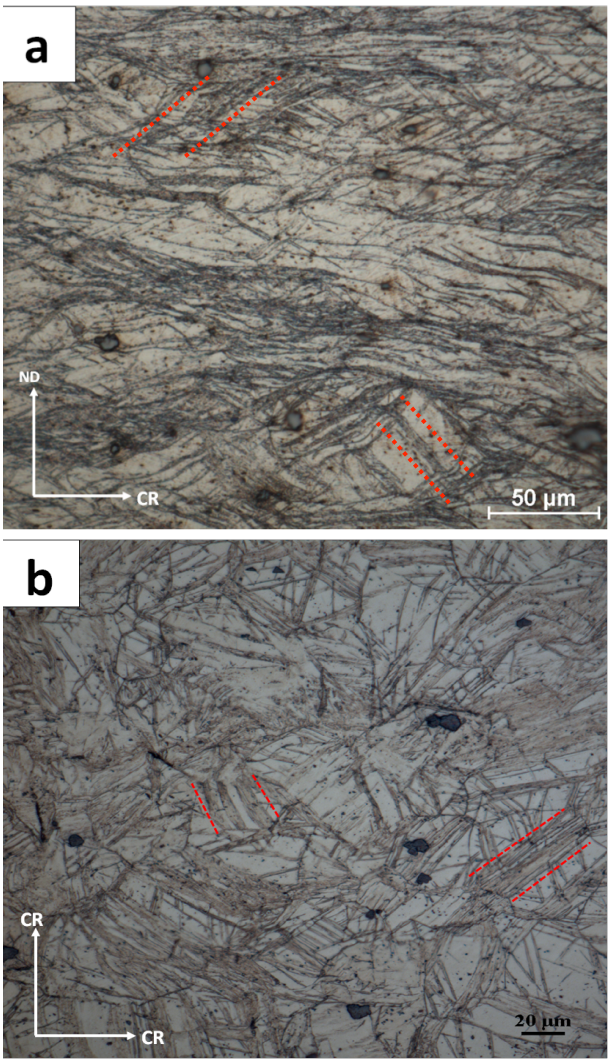

Fig. 2.3: Optical microstructures at the strain of 0.77 at high magnifications: (a) cross-section plane (ND-CR) and (b) cross-rolling plane (CR-CR). Band-like structures highlighted with red lines could be seen clearly.

2.3.2 EBSD

To gain a better insight into the early twinning events, EBSD observations were carried out on the low strain samples (Fig. 2.4). High quality maps could only be obtained for strains of 0.05 and 0.10. The maps confirm that most of the twins observed on the optical microscope, at a strain of 0.05, were {10-12} <10-11> extension twins in Fig. 2.4(a).

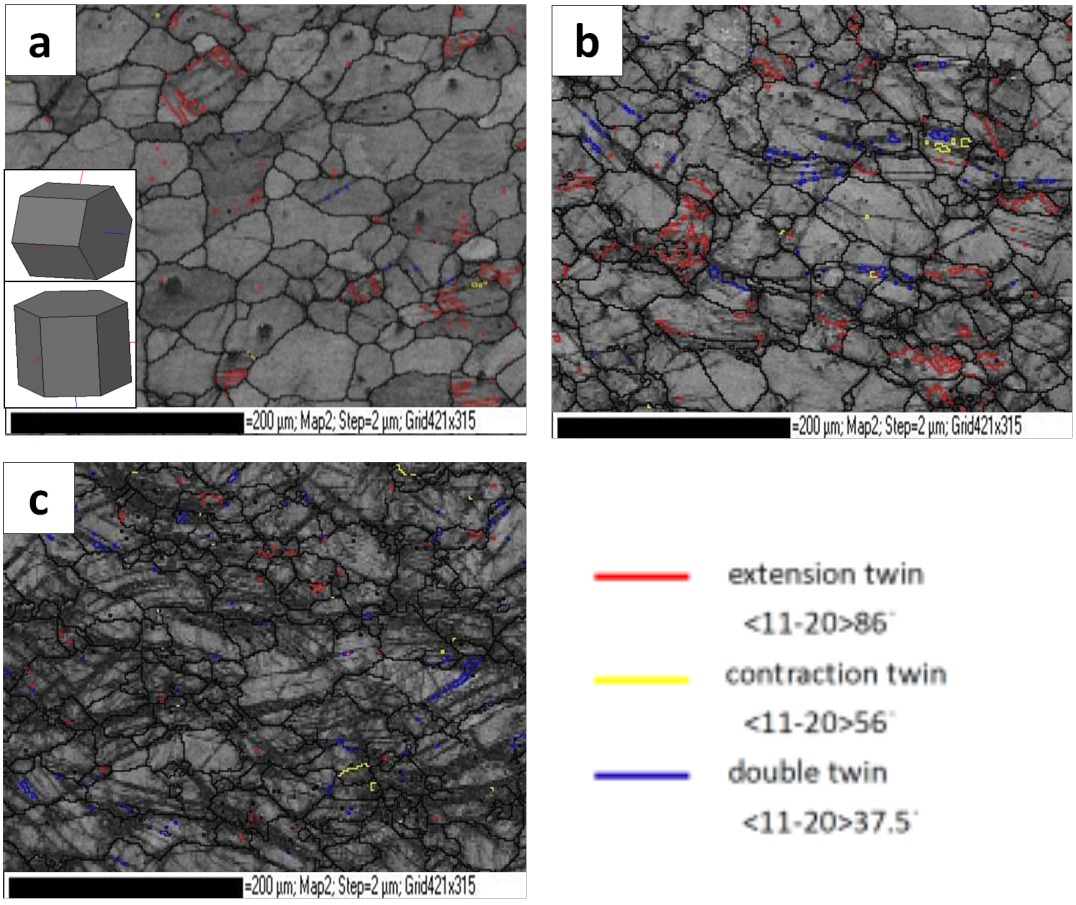

Fig. 2.4: EBSD Band Contrast Maps with twins at strains of (a) 0.05; (b) 0.10 and (c) 0.30. Three types of twins have been characterized with different colors.

Furthermore, these twins appear to form in grains whose c-axis is perpendicular to the normal direction of the sheet. The twinning of these grains strengthens the basal texture by rotating the basal planes by 86.3^{o}, thus making them parallel to the plane of the sheet, in agreement with earlier observations [5]. Further deformation to 0.10 revealed the presence of a significant number of {10-11}-{10-12} double twins as well as a few {10-11} <10-12> contraction twins in Fig. 2.4(b).

At a strain of 0.30, many regions with low Band Contrast (BC) appeared because of the high deformation in these regions. The presence of these regions suggests that some strain localization existed even in the 0.10 sample. Another important feature to be mentioned is that many fine scale twins still remained un-indexed; this is due to the 2μm step size used in EBSD mapping while plenty of twins were normally hundreds of nanometers in scale (discussed in TEM section).

2.3.3 TEM

Transmission Electron Microscopy was employed to examine the evolution of the dislocation structure and the development of fine scale twins that could not be observed by the EBSD technique.

Dislocation pile-ups were frequently observed at grain-boundaries (Fig. 2.5(a)). The representative dislocations structures taken under two beam diffraction conditions are shown in Fig. 2.5. The Burgers vector was analyzed by using 0002 and 01-10 reflections with <-2110> zone axis. Fig. 2.5(b) shows a bright field (BF) image taken by using 01-10 reflection; all dislocations, in contrast, are of either <a> or <c+a> type. Fig. 2.5(c) shows dislocations with a <c> component (<c> or <c+a> type) using 0002 reflection in the same area. <c+a> type of dislocations will be present in both reflections.

According to the analysis, it appears that development of <c+a> dislocation is very few at a strain of 0.05. From Fig. 2.5(b) it can be seen nearly all <a> type dislocations (invisible in Fig. 2.5(c)) are parallel to the basal trace indicating that majority of dislocations are basal dislocations. At the lowest strain (0.05), basal dislocations were the dominant features of the microstructure. Burgers vector analysis also revealed the presence of a small number of dislocations with a <c> component near grain-boundaries.

Extension twins of the type captured in the EBSD maps were also observed. In addition, it was possible to observe a small number of fine contraction twins. Twin-bundles, i.e. clusters of closely aligned fine scale twins, similar to the one shown in Fig. 2.7(a), were also found in very few cases. In all cases, the twins appeared to form at grain-boundaries and grew into the grains.

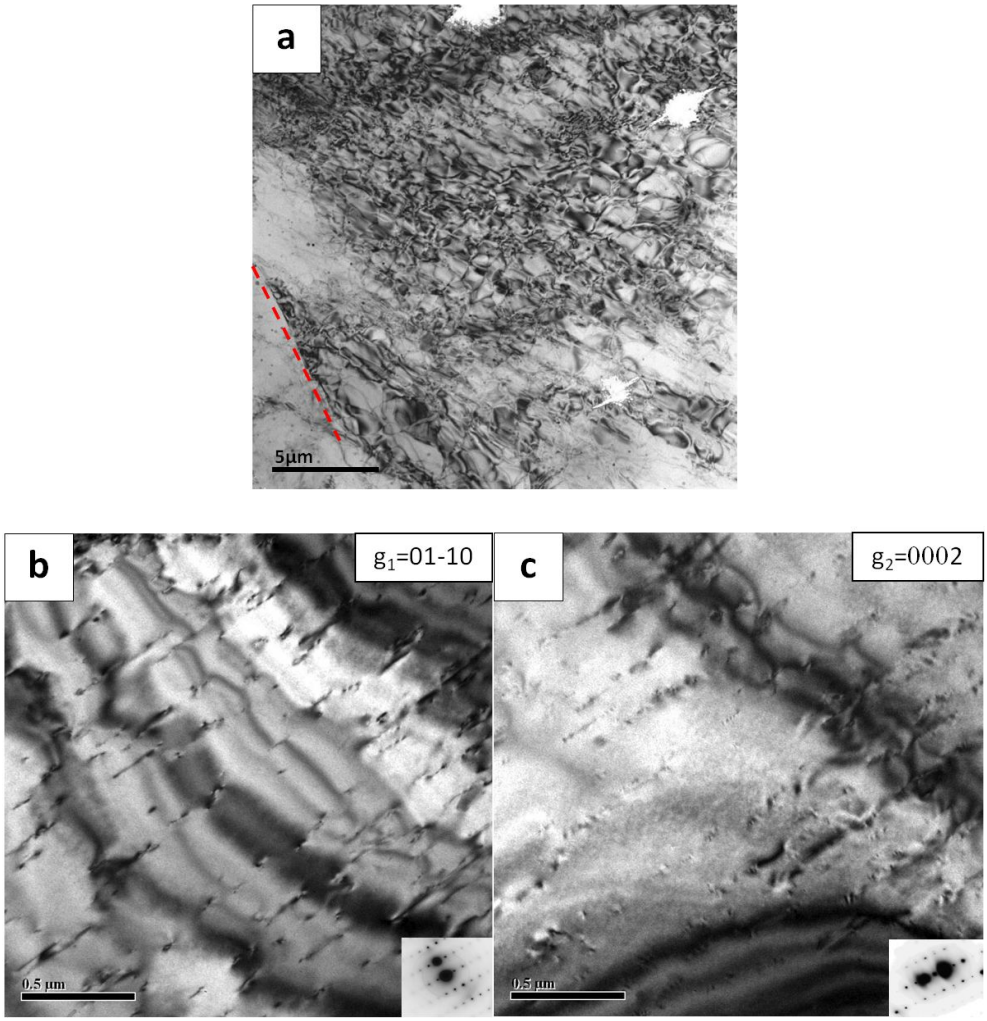

Fig. 2.5: TEM bright field images showing activity of basal dislocations at a strain of 0.05: (a) dislocations accumulated near grain boundary (shown at dotted red line); (b) g_1=01-10 reflection and (c) g_2=0002 reflection.

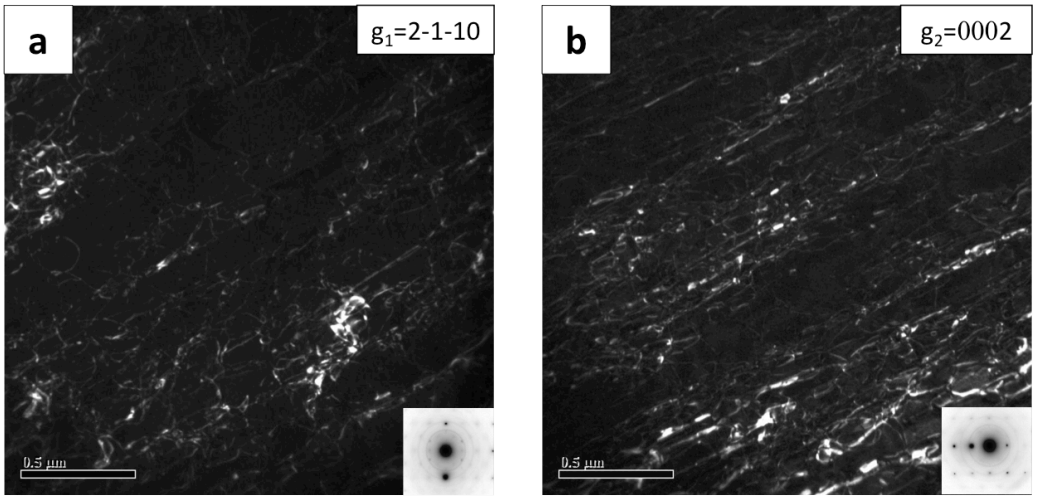

Fig. 2.6: TEM dark field images showing activity of <c> component (<c> or <c+a>) dislocations at a strain of 0.10: (a) g_1= 2-1-10 reflection and (b) g_2= 0002 reflection.

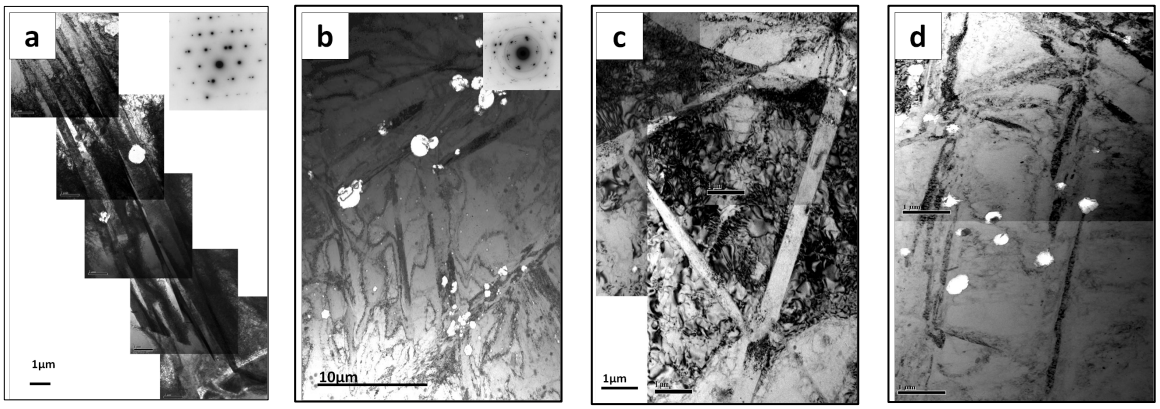

Fig. 2.7: Important microstructure features observed at various strains: (a) twin-bundles at a strain of 0.05; (b) double twins at a strain of 0.10; (c) dislocation cell wall structure at a strain of 0.30 and (d) twins with serrated boundaries at a strain of 0.30.

The dislocation structure at intermediate strains (0.10 and 0.30) was very heterogeneous, but on average the dislocation density was noticeably higher than that at a strain of 0.05. Burgers vector analysis revealed that an increasing number of the dislocations present were of the non-basal type (i.e. with a <c> component) as shown in Fig. 2.6. Dark field (DF) images were taken in the same area by using g=2-1-10 and g=0002 reflections. In Fig. 2.6(a), only <c+a> and <a> type dislocations were visible while only <c> and <c+a> dislocations showed up in contrast in Fig. 2.6(b). The dislocations appeared in both Fig. 2.6 (a) and (b) were then <c+a> dislocations. Qualitatively, non-basal dislocations were more abundant than those at a strain of 0.05.

As for the twinning evolution, the number of twins increased with strain and at a strain of 0.10, sets of twins were often observed within the same grain as shown in Fig. 2.7(b). A small number of twin-bundles similar to those shown in Fig. 2.7(a) were also observed. At a strain of 0.30, these twin-bundles became much more prevalent. The vast majority of the twins observed were double twins. Extension twins were rarely observed.

Two subtle features of the microstructure need to be pointed out: the first is the observation of dislocation cells in certain regions of the matrix as shown in Fig. 2.7(c). The presence of these structures is consistent with the activity of non-basal slip. It is also worth pointing out that some twin boundaries became serrated as shown in Fig. 2.7(d). This observation suggests that twins that formed at earlier stages of deformation are being sheared during subsequent straining.

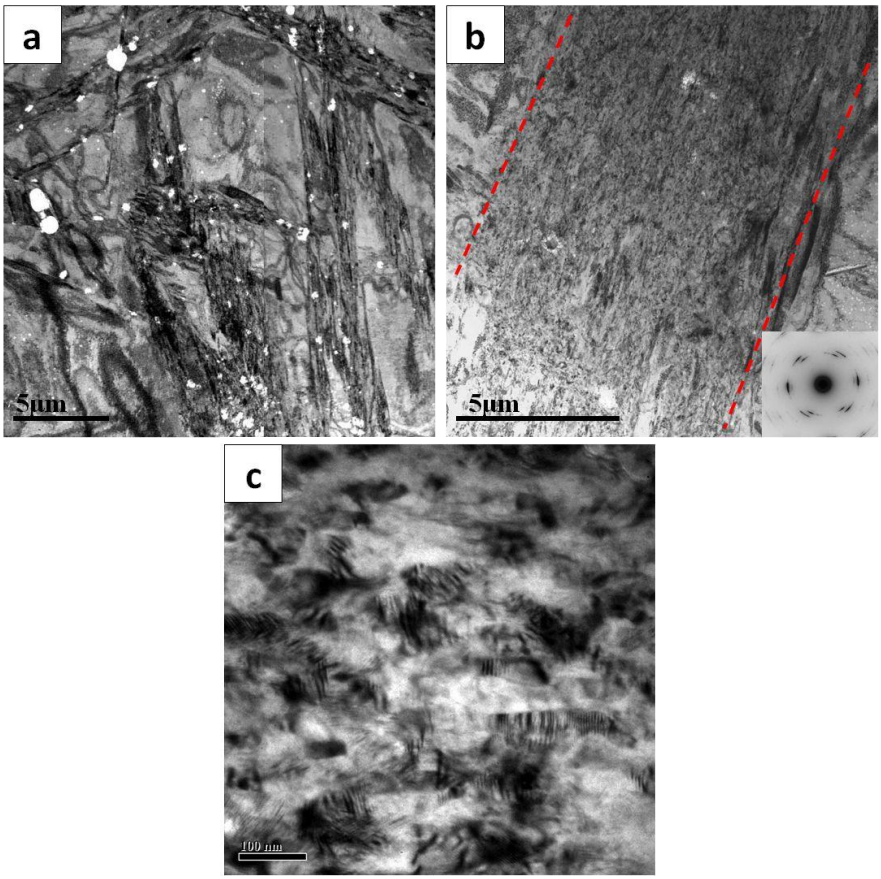

Fig. 2.8: (a) twin-bundles at a low magnification at a strain of 0.30; (b) individual twin-bundle at a strain of 0.77 and (c) detailed microstructure within the twin-bundle in (b) at high magnification.

Twin-bundles became the dominant feature of the microstructure at strains between 0.30 and 0.77 (Fig. 2.8(a)). The so-called band structure in OM section was actually the closely aligned twin structure/twin-bundles. These twin bundles contained high misorientations as suggested by the rings on the diffraction pattern (Fig. 2.8(b)). The twin-relation characteristic of twins on the {10-11} planes is still apparent on the diffraction pattern. The formation of rings on the diffraction pattern indicates that the

original twins were divided into smaller subgrains or grains with different orientations (Fig. 2.8(c)). Other researchers had already reported similar observations during the high-speed impact experiment [30].

The other important feature of the highly deformed samples was the development of shear bands. One such band was identified and selected using Focused Ion Beam milling (boxed area in Fig. 2.9). TEM examination of the band revealed that the highly deformed twin-bundles were found within the shear band region. Interestingly, even at the highest level of deformation areas of relatively low dislocation density could be observed. This is consistent with the strain being localized within the twin-bundles and shear bands.

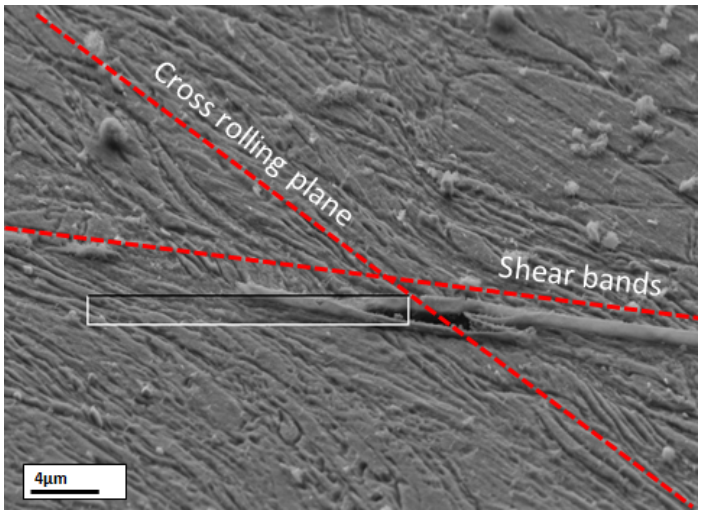

Fig. 2.9: SEM image showing the relationship between twin bundles and shear bands at the strain of 0.77. The cross-rolling plane and shear bands have been shown with red dotted lines.

2.3.4 Texture Evolution

In order to obtain a more global description of the microstructure and texture evolution, X-ray diffraction was utilized to construct {0002} pole figures. The data was plotted as a function of strain in Fig. 2.10. The as-received AZ31 sheet exhibited a relatively strong basal texture. With the cold cross-rolling, a strengthening of the basal texture could be noted up to a strain of 0.30. There was no noticeable change in texture beyond this strain.

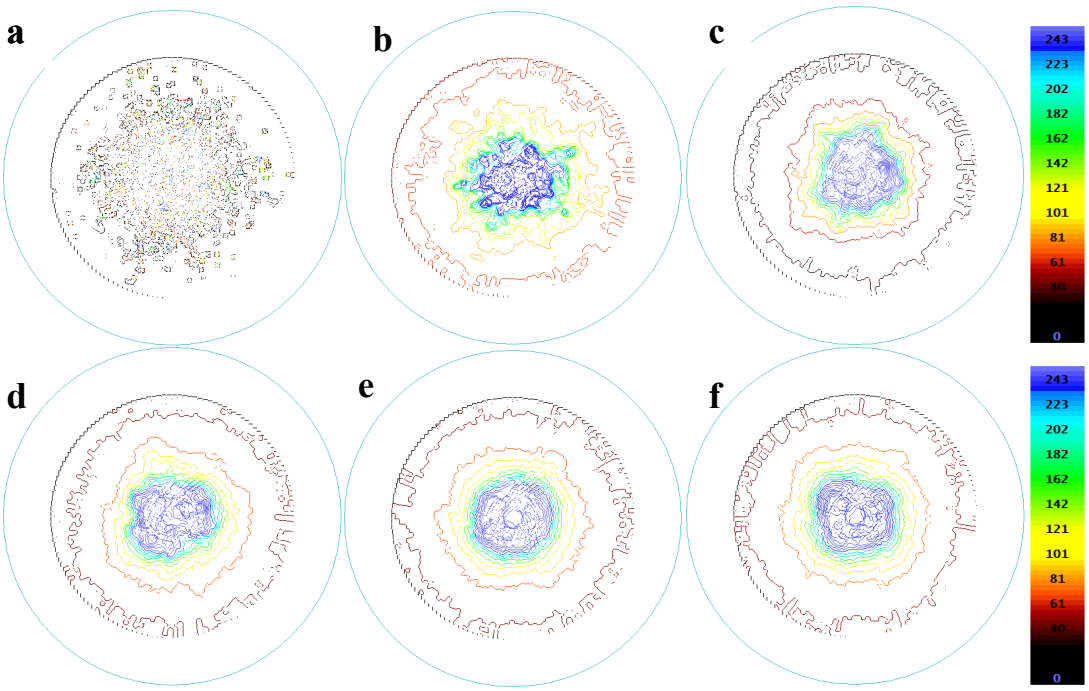

Fig. 2.10: {0001} pole figures of AZ31 cold rolled samples at strains of: (a) annealed; (b) 0.10; (c) 0.30; (d) 0.40; (e) 0.56 and (f) 0.77. Pole figures were plotted with respect to the raw experimental data.

2.3.5 Microhardness

The evolution of the microhardness with strain is summarized in Fig. 2.11. The hardness increases rapidly at low strains (e.g. 0~0.10). This was followed by a gradual increase for strains larger than 0.10. At a strain of 0.77, shear failure occurred at one end of the sample. Two kinds of cracks (parallel to dotted red lines) could be seen in Fig. 2.11 due to the shear banding on both cross sections and some micro-cracks could also be observed in these two directions.

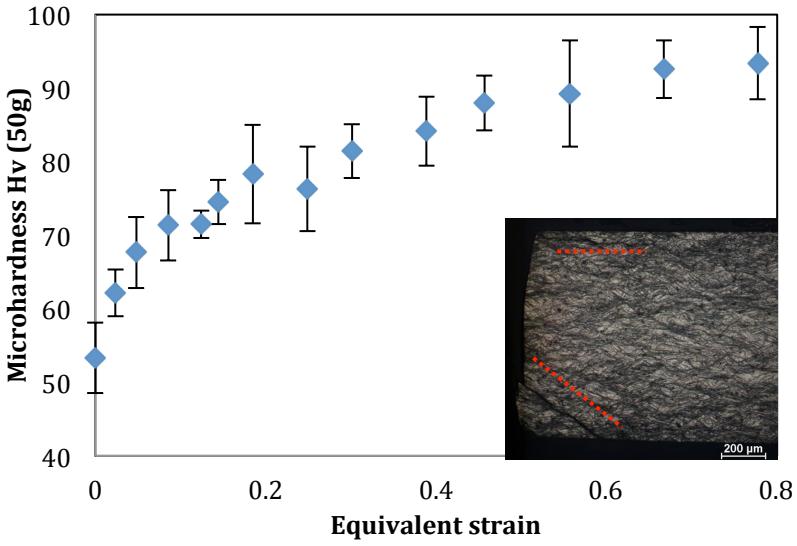

Fig. 2.11: Measured microhardness as a function of equivalent von Mises strain. A sample with shear failure at a strain of 0.77 is shown at the right-bottom. The cracks are parallel to the red dotted lines.

2.4. Discussion

2.4.1 Low Strains

A consistent description of the microstructure evolution of alloy AZ31 during cross-rolling is proposed based on the multi-scale observations reported in section 2.3. At the lowest strains (0.05) the main deformation mechanisms were basal slip and extension twinning. Fig. 2.5(b) and (c) show significant basal dislocation pile-ups near grain boundaries. A small number of <c+a> dislocations could be observed.

Extension twinning was the first type of twinning to be activated and it could be seen in a small number of grains at a strain of 0.05 (Fig. 2.4(a)). The grains which twinned had their c-axis perpendicular to the normal direction of the sheet and extension twinning within these grains reoriented the c-axis to a direction which is nearly parallel to the normal of the sheet. The occurrence of extension twinning in these grains is probably responsible for the strengthening of basal texture as well as a certain degree of texture hardening at the early stages of deformation.

Some authors argued that texture hardening caused by extension twinning should be responsible for the high initial work-hardening rate of Mg alloys [29, 33]. Knezevic et al [5], on the other hand, argued that the high work hardening rate is due to the progressive reduction of the mean-free path of <c+a> dislocations due to the formation of

a large number of fine scale twins. Our TEM work confirms the existence of these fine scale twins (Fig. 2.7(a)) as well as the operation of non-basal <c+a> slip. Quantitative modeling would be needed in order to determine which of the above mechanisms should be responsible for the high initial work-hardening rate.

In addition to extension twins, double twins as well as a small number of contraction twins were frequently observed at a strain of 0.10. The operation of these twin systems is essential in order to accommodate the c-axis strain during cross-rolling [8-9, 22, 33-34]. The twins varied in scale from hundreds of nanometers to several microns. In addition, <c+a> dislocations at this strain were more abundant than those at a strain of 0.05. Both observations are consistent with the fact that the CRSS for <c+a> slip and contraction/double twinning are much higher than those of basal slip and extension twinning [4, 21].

2.4.2 High Strains

At a strain of 0.30, more twins were present but they could not be indexed by EBSD. From the TEM analysis, twin clusters or bundles consisting of fine-scale double twins and contraction twins could be observed. Some of the twin boundaries appeared serrated and certain twins appeared bent, which suggests that these twins were sheared during subsequent deformation. The distortion of the twins, become increasingly more apparent at larger strains when strain-localization and shear-banding took place. Malin et al [31] had already reported that twins became "more wavy" in zinc sample cold rolled to a strain of 0.22.

At the highest strain of 0.77, the microstructure was dominated by the presence of a large number of the twin-bundles. These twin-bundles were constrained within the grain in which they formed. Globally, the key feature of the microstructure at this strain was the development of shear bands which ultimately led to the fracture of the sheet. The presence of both features is clearly seen in Fig. 2.9 which is a slightly-etched SEM image of the cross section, on which the deformed 'wavy' twins, the rolling plane, shear bands and associate micro-cracks are identified.

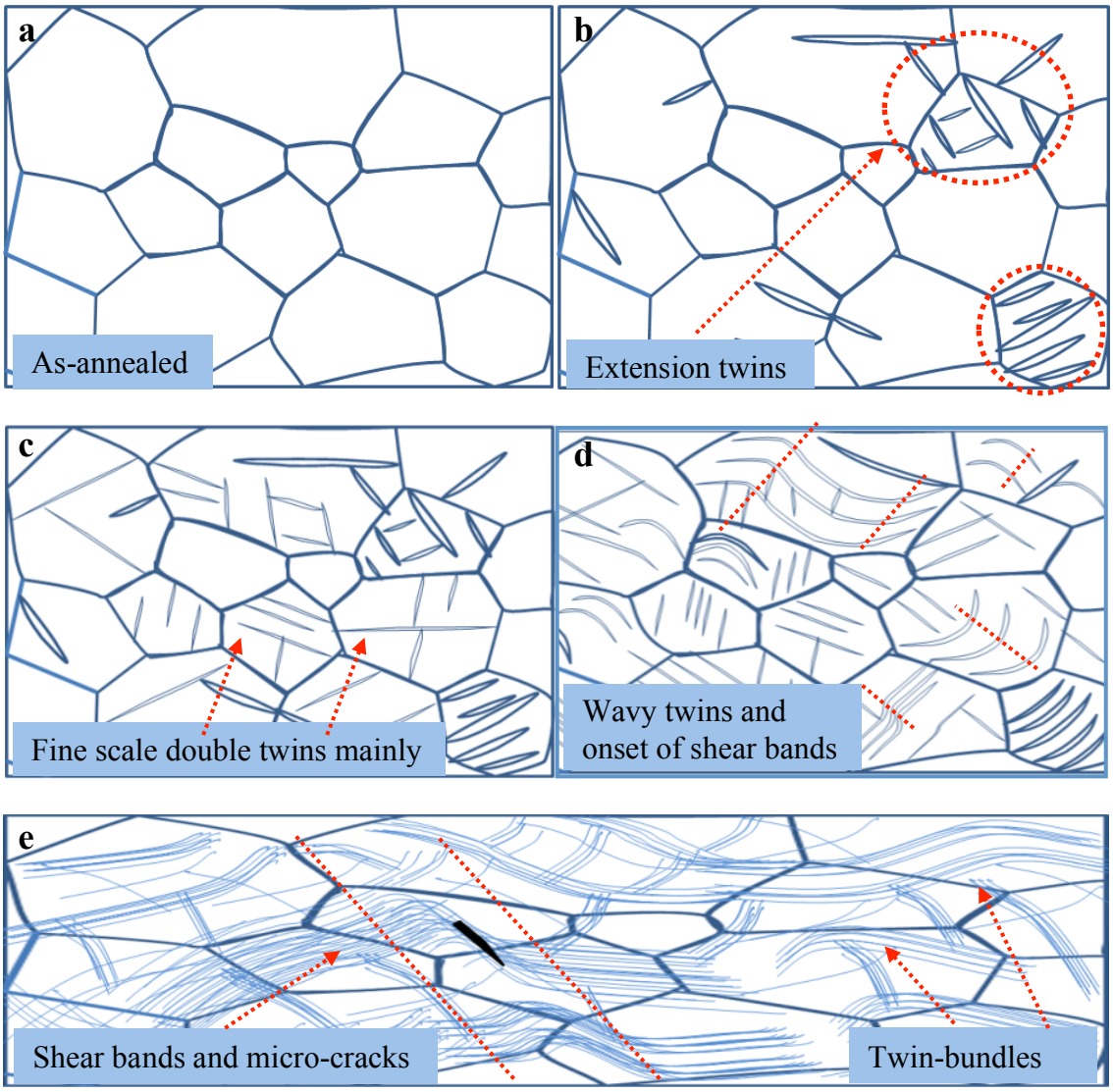

Fig. 2.12: Schematically drawn microstructure evolution of the deformed states at strains of: (a) as-annealed; (b) 0.05; (c) 0.10; (d) 0.30 and (e) 0.77.

2.4.3 Strain Localization

The term 'twin-bundle' is used to describe the closely aligned fine scale twins similar to those in Fig. 2.7(a) and 2.8. TEM diffraction analysis reveals that these are normally a mixture of double twins and contraction twins. The twin-bundles started forming at low strains (0.05~0.10) and their volume fraction increased with strain. Most of the twins present at strains of 0.30 or higher appeared to be belonging to a twin-bundle. The deformation within an individual grain appears to become increasingly more localized inside the twin-bundles. It should be emphasized that twin-bundles are crystallographic features and are therefore limited to grains in which they formed (i.e. they do not cross multiple grains). Twin-bundles appear to cause strain localization within the grain, in contrast to a shear bands which cause strain localization at a more macroscopic scale and cross multiple grains.

This distinction between twin-bundles and shear bands does not contradict the fact that shear-bands often contain a high number of twin-bundles. In fact, the TEM observation of Sandlobes et al [14] clearly show the presence of high number of twins in shear bands which was also consistent with our FIB-TEM observations. Another illustration of relationship and distinctions between twin-bands and shear bands is shown in Fig. 2.9 where a shear band cuts/shears the deformation twins and twin-bundles in its path.

Chapter 3: Static Recrystallization of AZ31

3.1 Introduction

Magnesium and many of its alloys readily develop strong texture during deformation. In the case of rolled sheets, the c-axis of the HCP unit cell aligns parallel to the normal of the sheet. This strong "basal" texture persists during subsequent processing and is found to limit the formability of the material [11, 25-26].

Interestingly, recrystallization does not significantly weaken the basal texture [10, 37]. The aim of this work is to identify the various recrystallization nucleation sites during the annealing of cold-rolled alloy AZ31 and to determine the orientation of the new nuclei formed and their contribution to texture evolution.

3.2 Experimental

3.2.1 Sample Preparation

Mg Alloy AZ31 (Mg-3%Al-1%Zn-0.4%Mn) was received in the form of 2.01 mm sheets. The as-received material was subjected to a homogenization treatment at 400^{o}C for 24 hrs, followed by a grain-growth treatment which consisted of a 5% cold-reduction

followed by annealing at 470^{o}C for 2 hrs. The resulting average grain size was in the range of 30 to 40 μm (referred to EBSD inverse pole figure in Fig. 2.1). The material was then cross-rolled at room-temperature to equivalent von Mises strains of 0.10 and 0.30. The rolling procedure consisted of a 0.03 mm reduction per pass and the rolling direction was rotated by 90^{o} after each pass.

Subsequently, the deformed samples were annealed at 250^{o}C and quenched into water at various times from 30s to 30mins in order to examine the evolution of recrystallization. All observations were carried out on the cross-section, well-below the surface. The only exception to this procedure is the sequence of images shown in Fig. 3.2. These images were obtained from the same specimen by observing the microstructure evolution on a polished surface as a function of annealing time.

3.2.2 Characterization Methods

The samples were examined using Optical Microscopy (OM), Scanning Electron Microscopy (SEM) and Transmission Electron Microscopy (TEM). The samples for optical metallography were prepared using standard metallographic methods followed by polishing with 9μm and 3μm diamond suspensions and 0.05μm colloidal silica solution (OPS). The grain boundaries were revealed using an etching solution of 6g picric, 100mL ethanol, 5mL acetic acid and 10mL water.

EBSD observations were performed on the as-polished material tilted 70^{o}, using a JEOL JSM-7000F FEG-SEM equipped with a CCD detector for EBSD analysis. An acceleration voltage of 20 keV and a working distance of 18.4 mm were used. The HKL Channel 5 software package was used to operate, acquire and analyze the data.

TEM foils were prepared by twin-jet electro-polishing at $-50^{o}C$ using a solution of 5.3g Lithium chloride, 11.16 g magnesium perchlorate, 500 mL methanol and 100 mL butyl Cellosolve and a voltage of 50 to 90V. Microstructure analysis was carried out on a PHILIPS CM12 transmission electron microscope, operating at 120kV.

3.3 Results

The as-deformed microstructure is described in detail in chapter 2. In what follows, emphasis is placed on the early stages of recrystallization.

3.3.1 Optical Microscopy

In the case of the samples that were deformed to a strain of 0.10, recrystallized grains were first observed within 10 to 30s of annealing (Fig. 3.1(c)). The predominant nucleation sites were twin/twin and twin/grain-boundary intersections; grain-boundaries, on the other hand, were not potential recrystallization nucleation sites under the present conditions. The recrystallization nuclei appeared to grow rapidly within the twinned regions but did not grow much into the matrix.

The recrystallization kinetics was significantly accelerated in the samples that were deformed to a strain of 0.30 by comparing Fig. 3.1(c) and Fig. 3.1(d). Once again, the predominant nucleation sites were twin/twin and twin/grain-boundary intersections. Recrystallization within twins was also observed, but not at grain-boundaries. The recrystallized nuclei became dominant even after 1000s annealing in Fig. 3.1(f) compared to 1800s annealing in Fig. 3.1(e). A more accurate recrystallization volume fraction is referred to the EBSD calculations in Table 3 in Appendix 1.

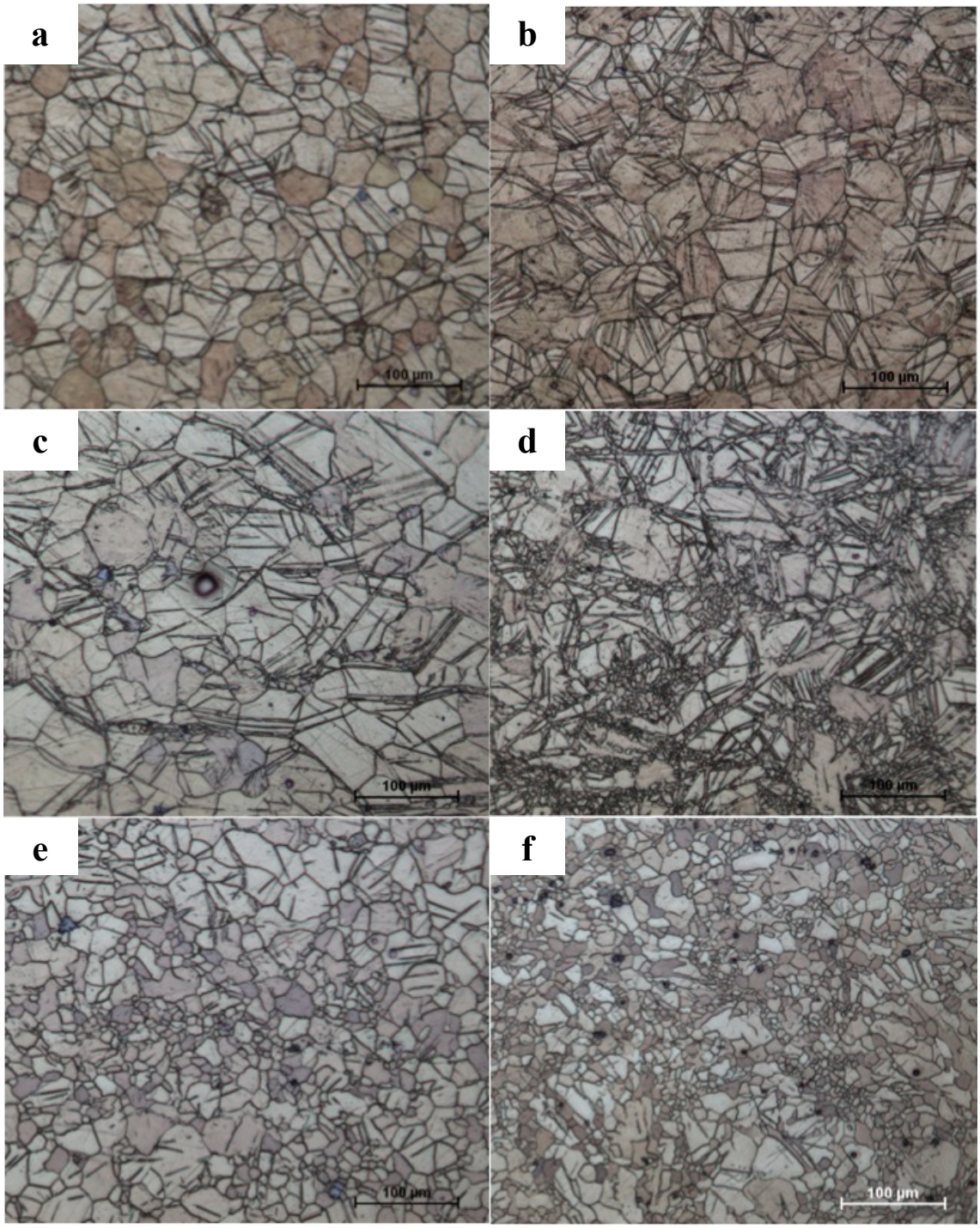

Fig. 3.1: Group A: Samples deformed to the strain of 0.10 and annealed: (a) deformed; (c) 250 ^{o}C for 30s; (e) 250 ^{o}C for 1800s; Group B: Samples deformed to the strain of 0.30 and annealed: (b) deformed; (d) 250 ^{o}C for 30s; (f) 250 ^{o}C for 1000s.

It should be pointed out, however, that a significant fraction of non-recrystallized material is retained between the recrystallized grains. These non-recrystallized regions persist within the microstructure even after long time annealing. An example of the microstructure evolution during annealing is shown in Fig. 3.2; nucleation within twins is evident. The arrows identify an example of the non-recrystallized regions that persist within the microstructure even after long time annealing [3].

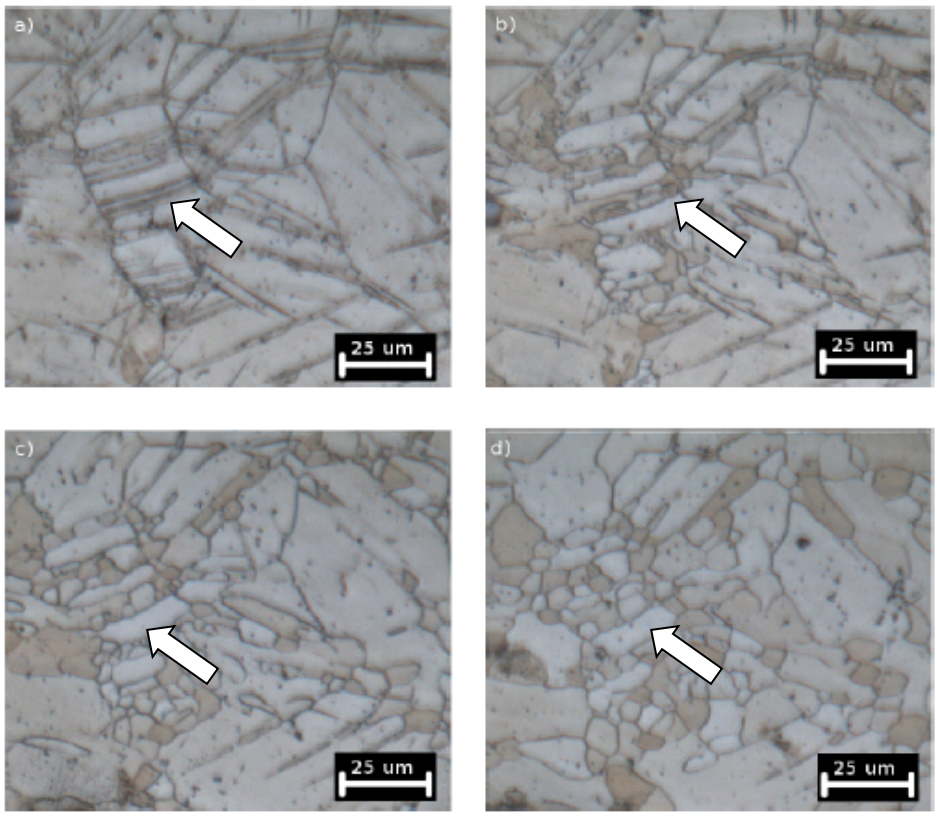

Fig. 3.2: Sequence of optical images by "in-situ" showing the evolution of recrystallization during annealing at 250 ^{o}C of a sample deformed to 0.30: (a) 5s; (b) 30s; (c) 100s and (d) 300s. Arrows highlight a region that did not recrystallize even after long time annealing [3].

3.3.2 EBSD

The use of EBSD allowed observation of recrystallization at a finer scale than that possible through optical metallography. Fig. 3.3 captures the early stages of recrystallization in a specimen that was deformed to a strain of 0.1 and annealed for 30s at 250°C. The recrystallized grains are readily identified by their small size. These observations confirm that nucleation occurs at twin/twin and twin/grain-boundary intersections. Grain-boundaries and twin interiors do not give rise to recrystallization at this strain.

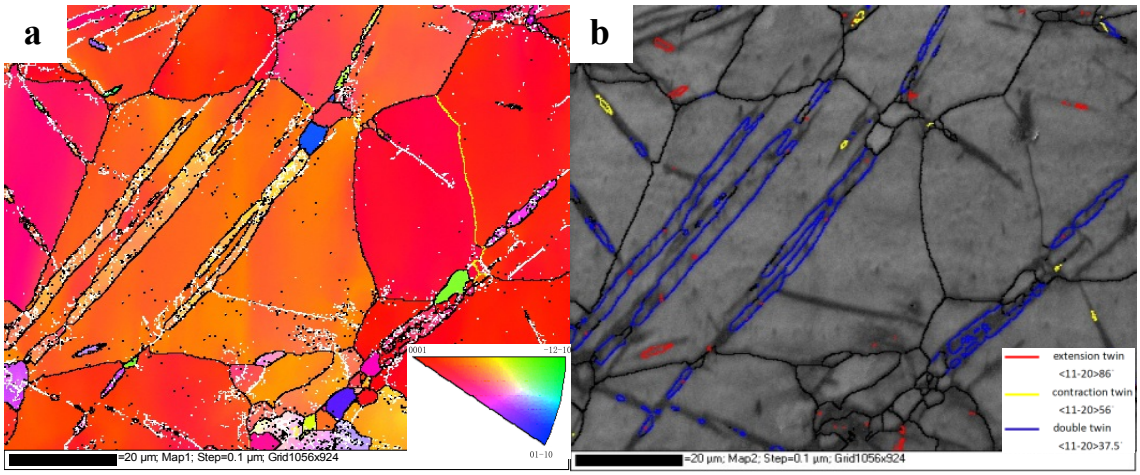

Fig. 3.3: (a) EBSD Inverse pole figure and (b) band contrast map of a sample that was deformed to the strain of 0.10 and annealed for 30s at 250 °C.

The microstructure of the specimens that were deformed to a strain of 0.30 could be divided into highly deformed regions which could not be indexed by EBSD and weakly deformed regions which are indexed and are shown to contain very small misorientations gradients.

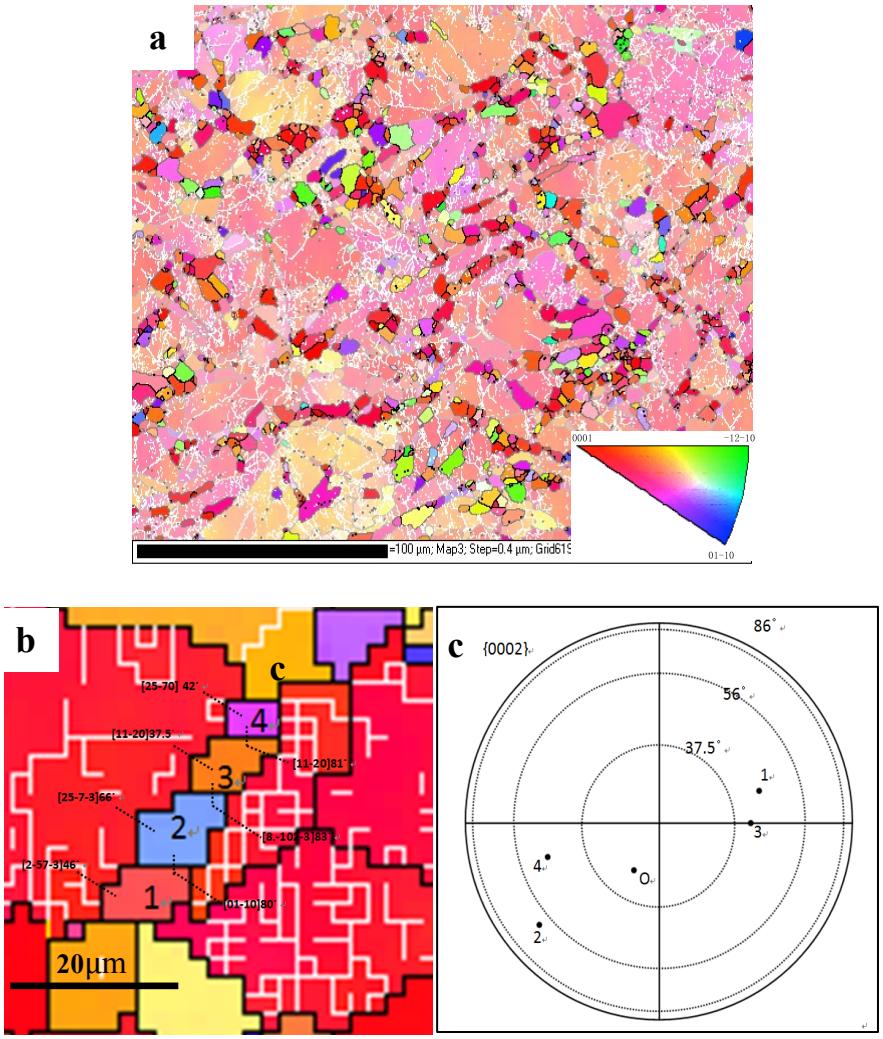

Fig. 3.4: (a) Inverse pole figure highlighting the recrystallized grains in a sample deformed to a strain of 0.3 and annealed at 250 ^{o}C for 30s; (b) a typical example of recrystallization in the twin and (c) the orientations of the recrystallization nuclei, number 1 to number 4, and related parent grain O.

The heterogeneity of the as-deformed microstructure is reflected in the spatial distribution of the recrystallization nuclei as shown in Fig. 3.4(a). These observations are consistent with those of earlier works [14, 39]. In addition to the nucleation sites described earlier, nucleation within the twins as well as nucleation at grain boundaries appeared to take place within the highly deformed regions.

An example of recrystallization within a twin is shown in Fig. 3.4(b). Detailed analysis of the orientations data indicates that grains 1 and 3 are close to the orientation of a double twin, {10-11}-{10-12}, while grains 2 and 4 had the orientation of a contraction twin {10-11}. This appears to be general trend as the vast majority of grains formed within the twins were found to be within few degrees of the double-twin or contraction twin orientation.

A global analysis of the orientation of the recrystallization nuclei is presented in Fig. 3.5 and Fig. 3.6, which are the pole figures for the unrecrystallized regions and recrystallized grains in the specimens deformed to strains of 0.10 and 0.30 and annealed for different amount of time. Interestingly, the texture of the recrystallized grains is significantly weaker than that of the unrecrystallized material, which is shown in Fig. 3.5(a) or Fig. 3.6(a) for comparison. The more detailed figures and analysis are present in the Appendix 1.

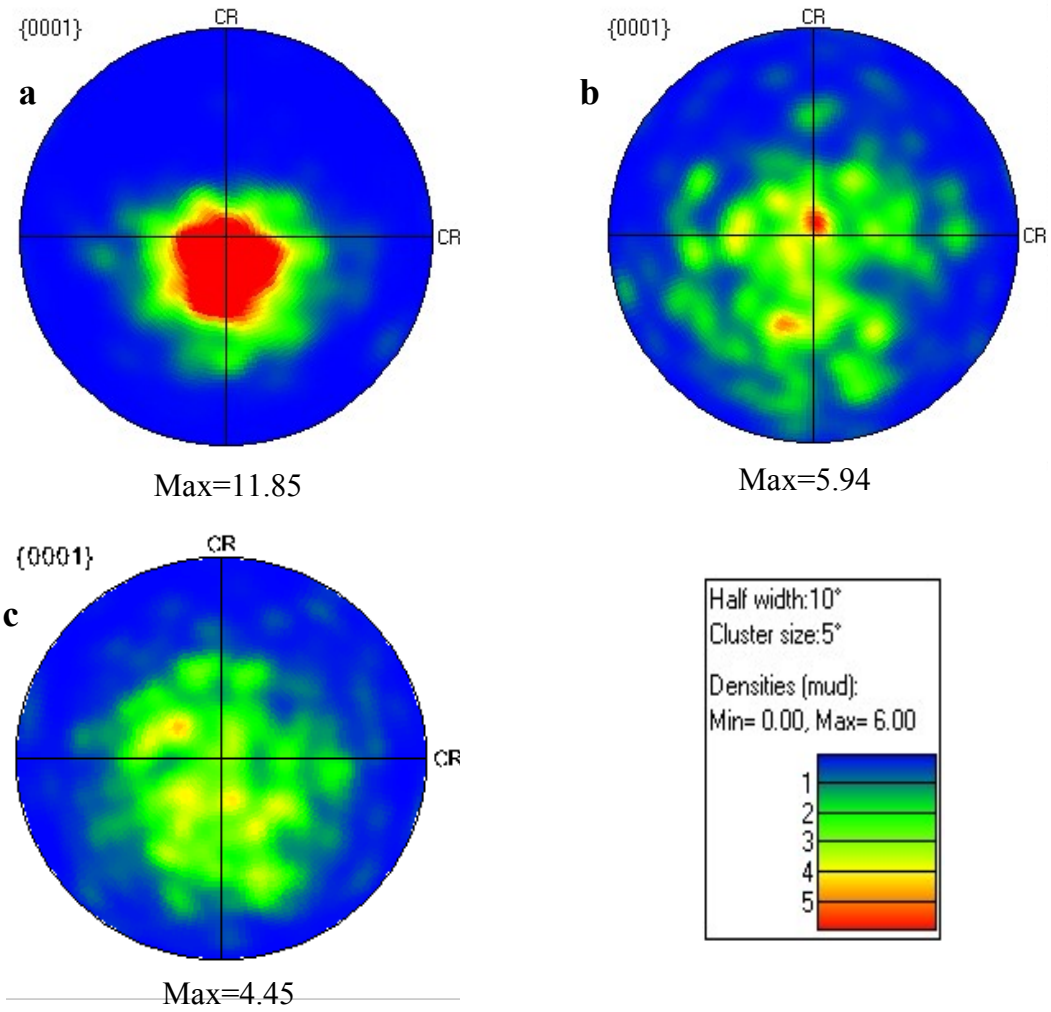

Fig. 3.5: (a) Pole figure of unrecrystallized regions of a sample deformed to 0.10 and then annealed at 250 ^{o}C for 30s; (b) pole figure of recrystallized nuclei of the same sample; (c) pole figure of recrystallized nuclei of a sample deformed to 0.10 and then annealed at 250 ^{o}C for 1800s.

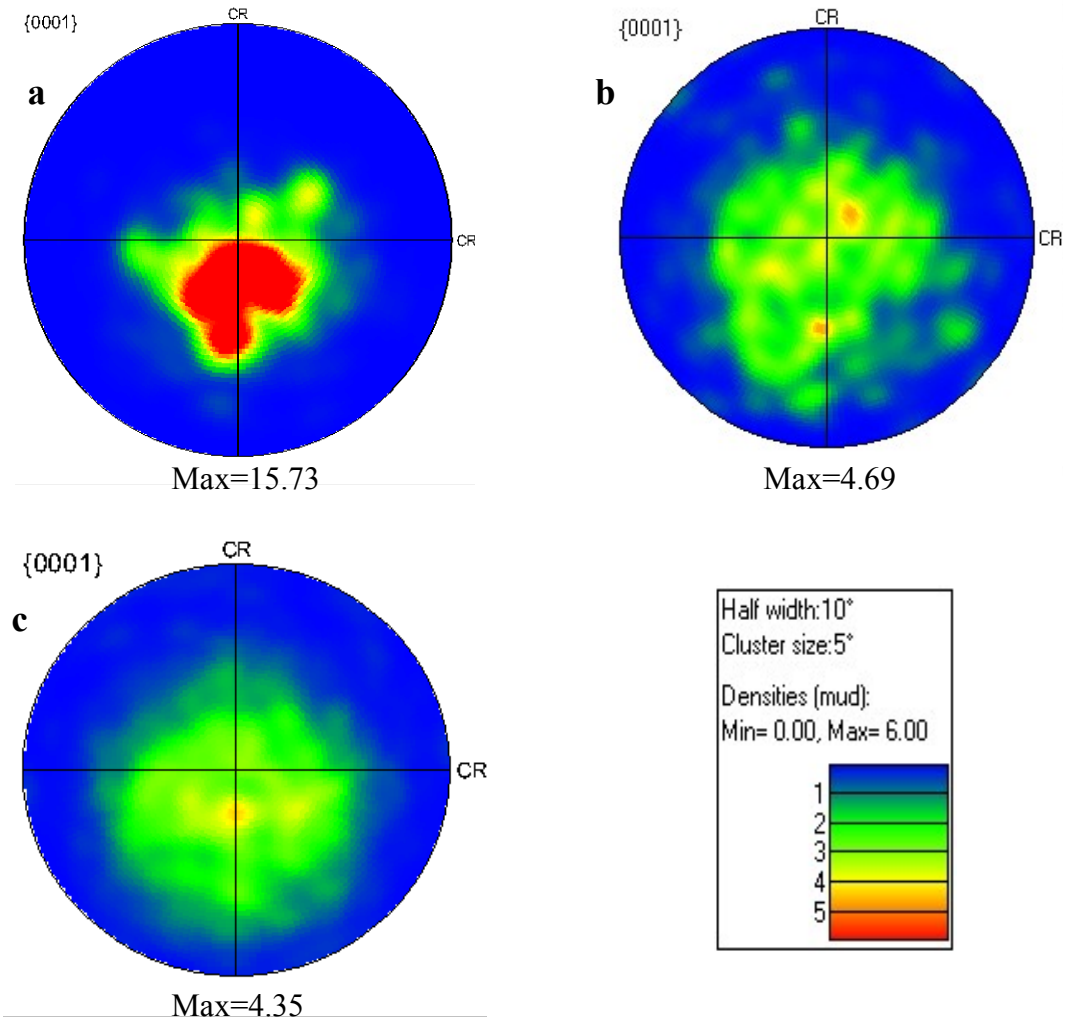

Fig. 3.6: (a) Pole figure of unrecrystallized regions of a sample deformed to 0.30 and then annealed at 250 ^{o}C for 30s; (b) pole figure of recrystallized nuclei of the same sample; (c) pole figure of recrystallized nuclei of a sample deformed to 0.30 and then annealed at 250 ^{o}C for 1000s.

3.3.3 TEM

Transmission electron microscopy observations reveal that extensive recovery occurs within the matrix and within the twins as shown in Fig. 3.7. The preferred nucleation sites for recrystallization are confirmed to be twin/twin and twin/grain-boundary intersections in the case of the specimens that were deformed to a strain of 0.10.

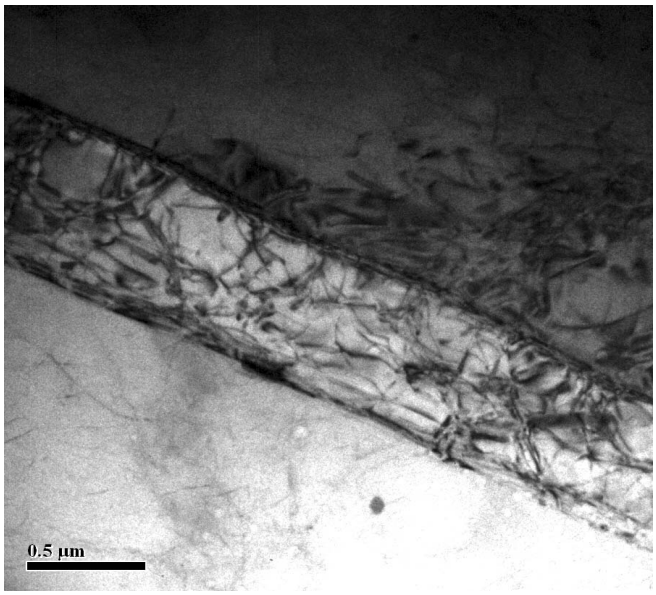

Fig. 3.7: Recovery in the matrix and the twin after annealing at 250 ^{o}C for 1800s of a sample deformed to 0.10.

The TEM observations clearly show that in addition to the important role played by twins in the 0.5 to 5µm range (as observed by EBSD), finer twins (<0.5 µm) appear to be important. The contribution of fine twins became increasingly more important at higher strain; Figs. 3.8(a, b) are examples of recrystallization nucleation at a cluster of fine twins.

Such twin bands/clusters were very commonly observed in the 0.30 samples. In one example the new grain grew into the twin band in Fig. 3.8(a), while in Fig. 3.8(b), the recrystallized grain appears to be growing into the matrix. Fig. 3.8(c) is an example of nucleation at the intersection of two fine twins that could not be detected by EBSD.

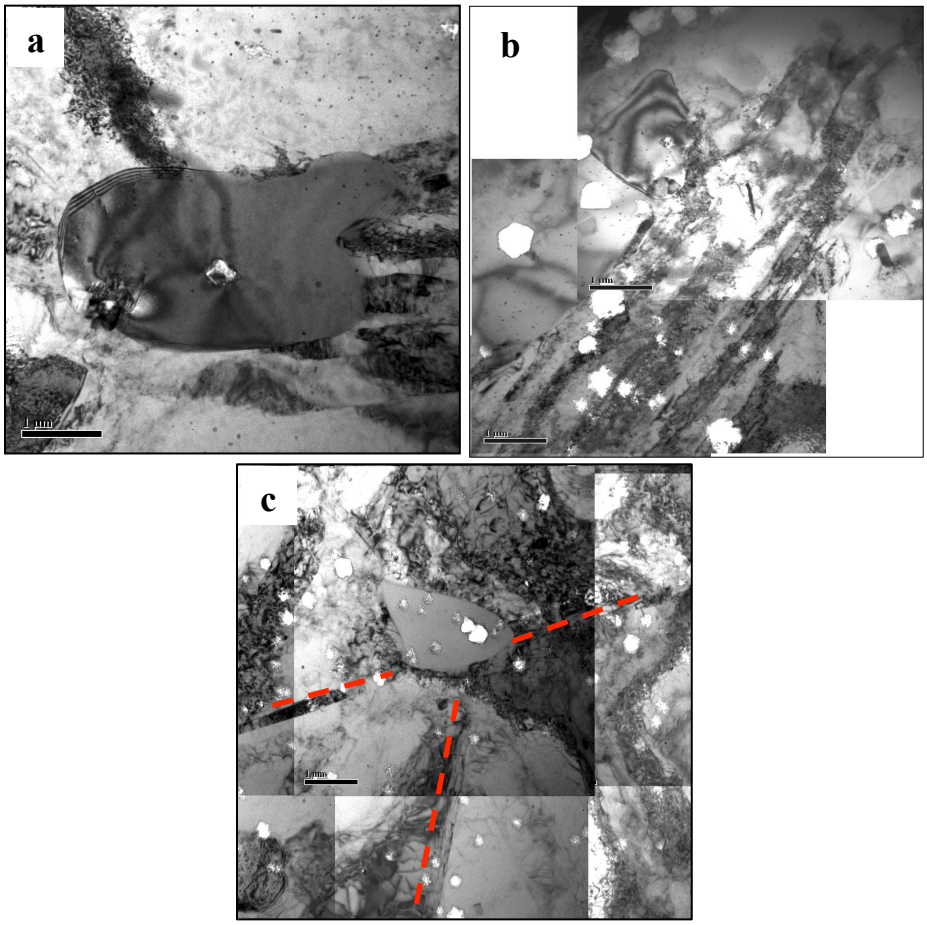

Fig. 3.8: TEM observations of recrystallization nucleation under various annealing conditions; (a) strain of 0.10, annealed for 30s, (b) strain of 0.30, annealed for 10s and (c) strain of 0.30, annealed for 30s.

3.4 Discussion

At small strains, ε=0.10, twin/twin and twin/grain-boundary intersections appear to be the predominant recrystallization nucleation sites; grain-boundaries do not appear to be effective nucleation sites. Nucleation at these sites appears to generate new (non-basal) orientations as shown by the pole figure constructed using data from only the recrystallized grains (Fig. 3.5 (b and c)). The global texture, however, is not changed significantly because the recrystallized fraction stagnates at low volume fraction due to the low stored energy and fast-recovery in the as deformed microstructure.

At higher strains (0.30), the as-deformed state becomes increasingly more heterogeneous; the microstructure could be divided into highly deformed bands, which could not be indexed by EBSD and weakly deformed regions, which are indexed and are shown to contain very small misorientation gradients. Nucleation sites are relatively complicated within the highly deformed regions due to the complex as-deformed microstructure.

The activation of nucleation within twins leads to new grains that are rotated by 5 to 10^{o} from the contraction or double-twin orientations. This has the effect of broadening the basal texture, but it does not lead to new orientations that are dramatically different from those of the as-deformed state, which is in agreement with the conclusions reached by [38]. Similarly, the activation of grain-boundary bulging within the highly deformed regions appears to preserve the basal texture because the bulging grain possesses an

orientation that is close to that of the grain from which it bulged. A detailed discussion on the recrystallization nucleation mechanism has been carried out in Appendix 2.

A third factor, which contributes to the retention of basal texture during the annealing of AZ31, is the absence of recrystallization within a significant fraction of the microstructure. EBSD and TEM observation suggest that the weakly deformed regions of the microstructure contain simple planar dislocation structures. These recover rapidly during annealing thus depleting the driving force for recrystallization in these regions. As a result of these factors, recrystallization in AZ31 only leads to the weakening of the basal texture; it is not possible to completely eliminate the basal texture.

Chapter 4: Conclusions

4.1 Deformation

The microstructure evolution of alloy AZ31 as a function of strain was observed over a wide range of length scales. Fig. 2.12 is a schematic diagram depicting the key steps of microstructure evolution reported here:

1. $\varepsilon \leq 0.05$. Basal plane slip is the first deformation mode to be activated. Extension twinning is also observed in grains that are favorably oriented. Small amount of <c+a> slip as well as few double/contraction twinning takes place near grain boundaries due to stress concentrations associated with dislocation pile-ups and incompatibility strains. The interaction between slip and twinning might be responsible for the high work hardening rate of Mg alloy.

2. $\varepsilon = 0.05 \sim 0.10$. More <c+a> type dislocations could be observed compared to stage (1). Basal slip might be more difficult due to the hard orientation of crystals at this stage. Double twinning occurs. The basal texture is strengthened up to a strain of 0.10.

3. $\varepsilon = 0.10 \sim 0.30$. Twinning continues as the strain increases and many fine scale twins as well as local twin-bundles could be seen. The formation of twin-bundles leads to

strain localization within the grains. Evidence of global/macroscopic strain localization could also be seen in EBSD maps and optical images at a strain of 0.30.

4. ε= 0.30~0.77. In the high strain stage, the dislocation density is too high to conduct dislocation analysis. The most important features are the increasing volume fraction of twin-bundles and the further development of shear bands. The absence of work hardening over this strain range is linked to the severe localization of deformation. The strong basal texture still maintains at this stage. Micro-cracks and shear failure could be observed in the vicinity of shear bands at strain of 0.77.

4.2 Recrystallization

1. Recovery of magnesium is relatively fast, which consumes driving force, i.e. the stored energy, rapidly and leads to the incompletion of recrystallization. Ways that could reduce the stacking fault energy, such as adding specific elements, might be able to slow down the recovery process;

2. Recrystallization nucleation occurs at intersections of twin/twin or twin/grain-boundary and within twins, nucleation events within the matrix and at grain-boundaries are very rare;

3. The orientations of the recrystallization nuclei are relatively random; recrystallization could be the way to change the basal texture or at least weaken the basal texture. But, again, this idea might be inhibited by the incompletion of recrystallization.

Chapter 5: Future Work

5.1 Deformation

With the benefit from the process of cross-rolling, the sample could be deformed to an equivalent strain of 0.77. Even though a large amount of work has been conducted on the deformation of alloy AZ31 during last almost two years, certain areas still require further investigation. In particular, the formation of twin-bundles and the effect of these on the work hardening are not well understood at this moment. Quantitative analysis of these twin-bundles should be conducted in the near future, i.e. the morphology, volume fraction and global distribution of the twin-bundles. This information would be critical for estimating the way in which twinning modifies the mean-free path for dislocation slip and the evolution of the yield stress and work-hardening rate.

5.2 Recrystallization

Due to the crystallography of HCP materials, the formation of strong basal texture is inevitable during deformation, which limits the formability of magnesium alloys. Subsequent annealing might be the way to change the strong basal texture. From our current results of recrystallization nucleation of AZ31, the texture of the nuclei is relatively random compared to the deformed sample. The growth of the nuclei is retarded by the rapid recovery. Therefore, several experiments could be pursued in the future:

1. Repeating the low-strain deformation and annealing: It was observed that a sample deformed to the strain of 0.10 and annealed at 250 ^{o}C for 1800s would form a large number of nuclei within twins and at intersections of twin/twin and twin/grain-boundary. If the sample is then deformed to an additional strain of 0.10 many twins and intersections of twin/twin and twin/grain-boundary would form in the matrix, but not within the preexisting nuclei because of their small size. Thus, another group of nuclei will form in the matrix and the old ones would grow into the matrix by the new driving force. A random texture could be developed by the repeated deformation and annealing.

2. Developing the new magnesium alloys: One of the most important parameters, which control the recovery process, is the stacking fault energy. SFE varies depending on the alloy elements. We may be able to develop a new magnesium alloy by adding specific elements, such as rare earth elements which reduce the rate of recovery.

References

[1] C.J. Bettles, M.A. Gibson, JOM 57 (2005) 46–49.

[2] P. Greenfield, Magnesium, Mills &Boon Limited, London, 1972.

[3] P. Okrutny, Master's thesis, McMaster University, 2010.

[4] Fumiaki Hiura. Master's thesis, McMaster University, 2010.

[5] Marko Knezevic et al., Acta Materialia 58 (2010) 6230–6242.

[6] P. G. Partridge. Metallurgical Reviews, (1967) 169-194.

[7] A. Kelly, G.W. Groves and P. Kidd. CRYSTALLOGRAPHY and CRYSTAL DEFECTS, Revised Edition, JOHN WILEY&SONS, LTD, 2000.

[8] W. H. Hartt and R. E. Reed-Hill. Trans. Metall. Soc. AIME, 1967; 239:1511.

[9] B. C. Wonsiewicz and W. A. Backofen. Trans. Metall. Soc. AIME, 1967; 239:1422.

[10] Y.N. Wang, J.C. Huang. Materials Chemistry and Physics 81 (2003) 11–26.

[11] U.F. Kocks, C.N. Tome and H.R. Wenk. Texture and Anisotropy: Preferred Orientation in Polycrystals and Their Effect on Materials Properties, Cambridge University Press, Cambridge, 1998.

[12] A. Styczynski, Ch. Hartig, J. Bohlen and D. Letzig. Scripta Materialia 50 (2004) 943–947.

[13] F. J. Humphreys and M. Hatherly. Recrystallization and Related Annealing Phenomena. Pergamon, Oxford, 1996.

[14] S. Sandlobes et al. Acta Materialia 59 (2011) 429–439.

[15] H. Miura, G. Yu and X. Yang. Mater. Sci. Eng. A 528 (2011) 6981.

[16] W. C. Liu, X. Y. Li and X. C. Meng. Scripta Materialia 60 (2009) 768–771.

[17] L.E. Murr. Interfacial Phenomena in Metals and Alloys. Addison-Wesley, Reading, 1975, p 131.

[18] C.W. Su, L. Lu, and M.O. Lai. Philosophical Magazine, 88 (2008) 181-200.

[19] C.S. Roberts. Magnesium and Its Alloys, John Wiley & Sons, Inc., New York, 1960, pp. 81-107.

[20] C. S. Barrett. Structure of Metals. New York: McGraw-Hill; 1952.

[21] J. Koike et al, Acta Mater., 51 (2003) 2055-2065.

[22] J.J. Jonas et al, Acta Mater., 59 (2011) 2046-2056.

[23] Yoo MH. Metall. Mater. Trans. A., 12 (1981) 409.

[24] Z. Keshavarz, M.R. Barnett. Scripta Mater., 55 (2006) 915.

[25] T. Al-Samman, G. Gottstein, Mater. Sci. Eng. A, 488 (2008) 406-414.

[26] M.D. Nave, M.R. Barnett, Scripta Mater., 51 (2004) 881-885.

[27] S.H. Parka et al, Mater. Sci. Eng. A, 532 (2012) 401-406.

[28] Y.C. Xin et al, Mater. Sci. Eng. A, 532 (2012) 50-57.

[29] M.R. Barnett. Mater. Sci. Eng. A, 464 (2007) 1-7.

[30] D.L. Zou et al, Materials Characterization, 62 (2011) 496-502.

[31] A.S. Malin, M. Hatherly and V. Piegerova. (1982b), Proc. 6th Int. Conf. on Strength of Metals and Alloys, ed. Gifkins, Pergamon, Oxford, 523.

[32] B.J. Duggan, W.B. Hutchinson and M. Hatherly. (1978b), Scr. Met.12,1293.

[33] E.W. Kelley, W.F. Hosford and Jr. Trans. Metall. Soc. AIME, 1968; 242:5.

[34] P. Yang et al. Scripta Mater., 50 (2004) 1163–1168.

[35] U.F. Kocks. popLA: preferred orientation package-Los Alamos, October, 1995.

[36] MTEX software package referred to: http://code.google.com/p/mtex/downloads/list.

[37] J.Y. Lia, J.F. Wang, D.L. Zhang and X.K. Wang. Materials Science Forum Vol. 686 (2011) 101-106.

[38] X. Li, P. Yang, L.N. Wang, L. Meng and F. Cui, Materials Science and Engineering A 517 (2009) 160–169.

[39] M. Dzubinsky, Z. Husainb and W.M. van Haaften. Materials Characterization 52 (2004) 93–102.

Appendix 1

EBSD Characterization on Recrystallization

The EBSD Inverse Pole Figures for the recrystallization nuclei[4] are shown here and the nuclei are highlighted by coloring the matrix grey. The annealing conditions are 10% deformed and annealed at 250 ^{o}C for 30s and 1800s, respectively; 30% deformed and annealed at 250 ^{o}C for 30s and 1000s, respectively. The corresponding figures are shown from Fig. A1 to Fig. A4.

A recrystallization volume fraction was calculated from EBSD data. Semi-quantitatively, the "Basal"[5] nuclei volume fraction was also calculated for comparison. We found that about two thirds of the recrystallized nuclei is non-basal oriented, which is important to the understanding of recrystallization texture evolution.

Table 3: Summary of Recrystallization Volume Fraction by EBSD

	Recrystallization volume fraction	"Basal" nuclei volume fraction
10%_250 ^{o}C_30s	~3%	~1%
10%_250 ^{o}C_1800s	~23%	~6%
30%_250 ^{o}C_30s	~24%	~8%
30%_250 ^{o}C_1000s	~58%	~21%

[4] The recrystallized nuclei were defined by the mean misorientation within a grain. If the mean misorientation within a grain is less than 1^{o}, then the grain is treated as the recrystallized nucleus after annealing. One thing to be pointed out is the mean misorientation threshold value is variable, further information referred to [39].

[5] The "basal" orientation of the {0001} pole is defined as a circle region that is about 25 ^{o} away from the center point. The nuclei formed within this region are of great interest to the study of recrystallization.

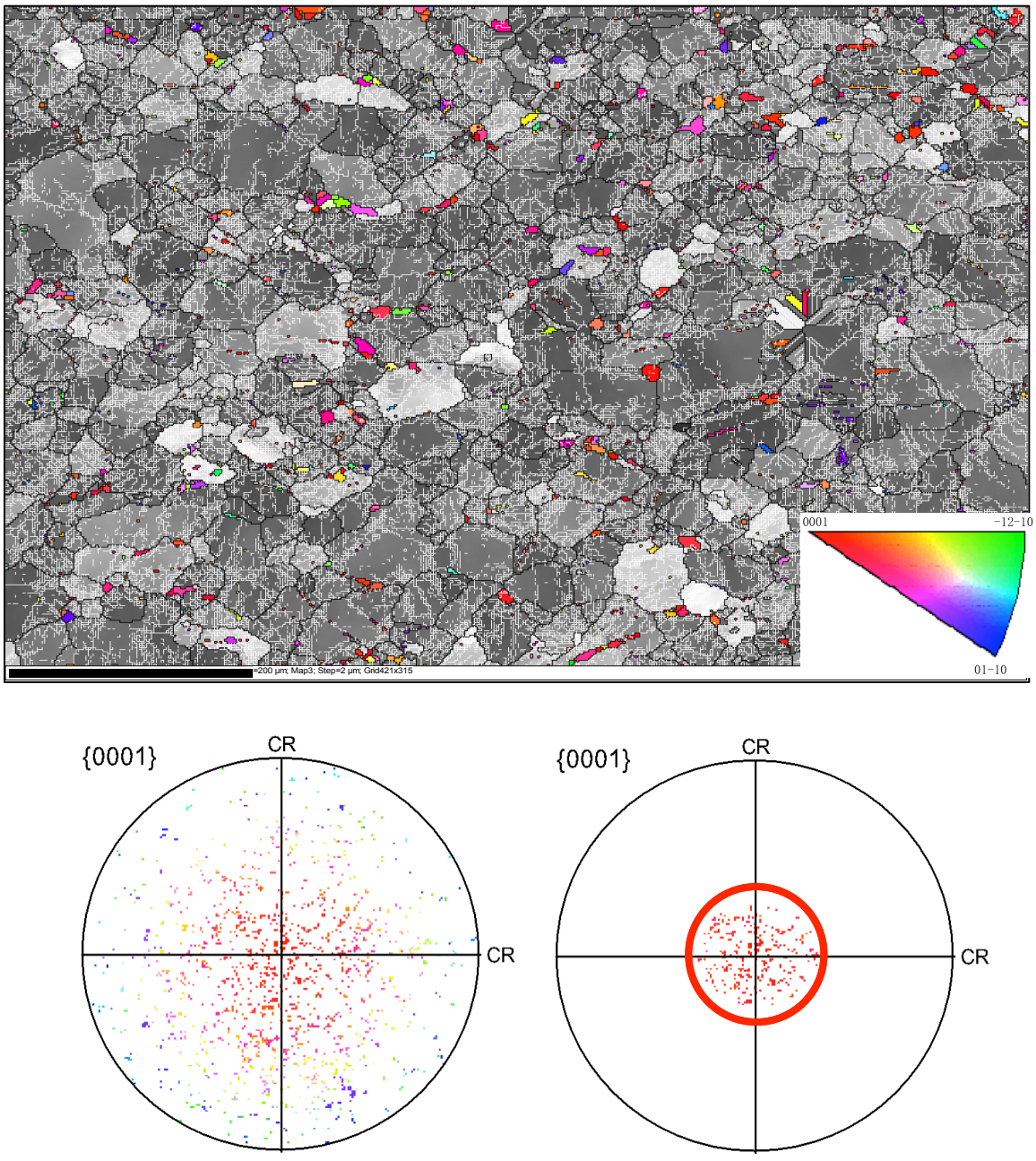

Fig. A1: Recrystallized nuclei orientation analysis of a sample that was 10% deformed and annealed at 250 ^{o}C for 30s.

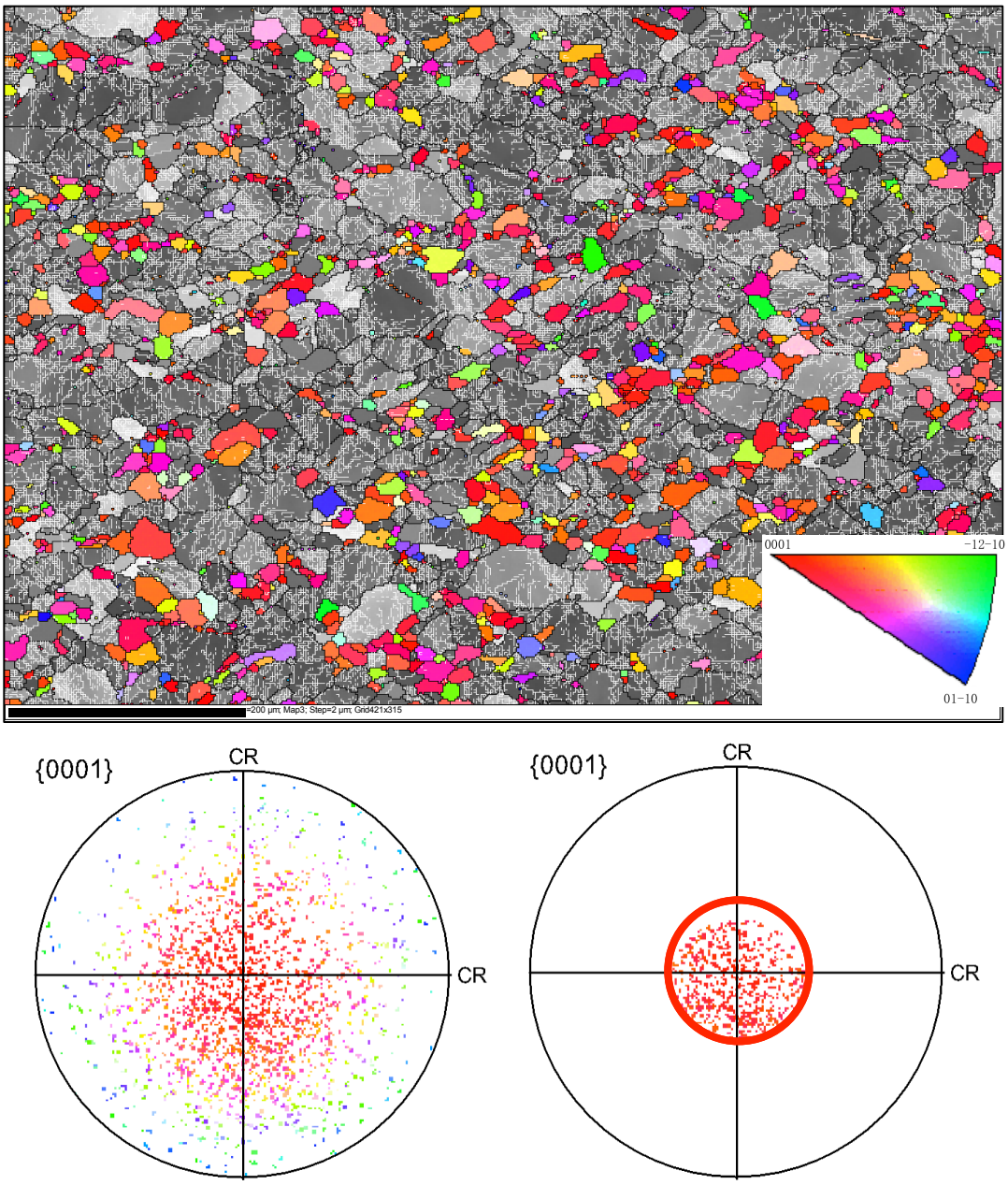

Fig. A2: Recrystallized nuclei orientation analysis of a sample that was 10% deformed and annealed at 250 ^{o}C for 1800s.

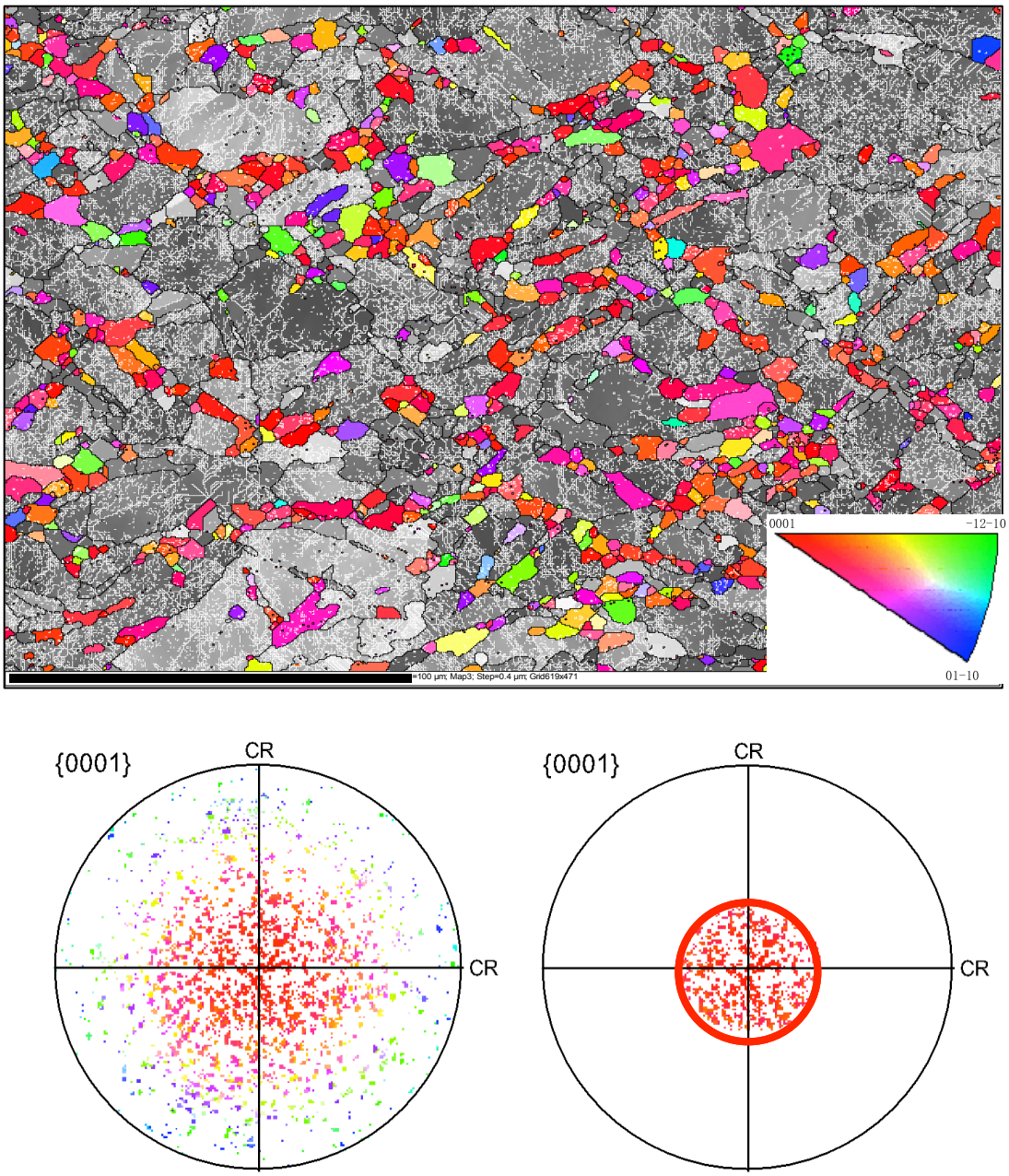

Fig. A3: Recrystallized nuclei orientation analysis of a sample that was 30% deformed and annealed at 250 ^{o}C for 30s.

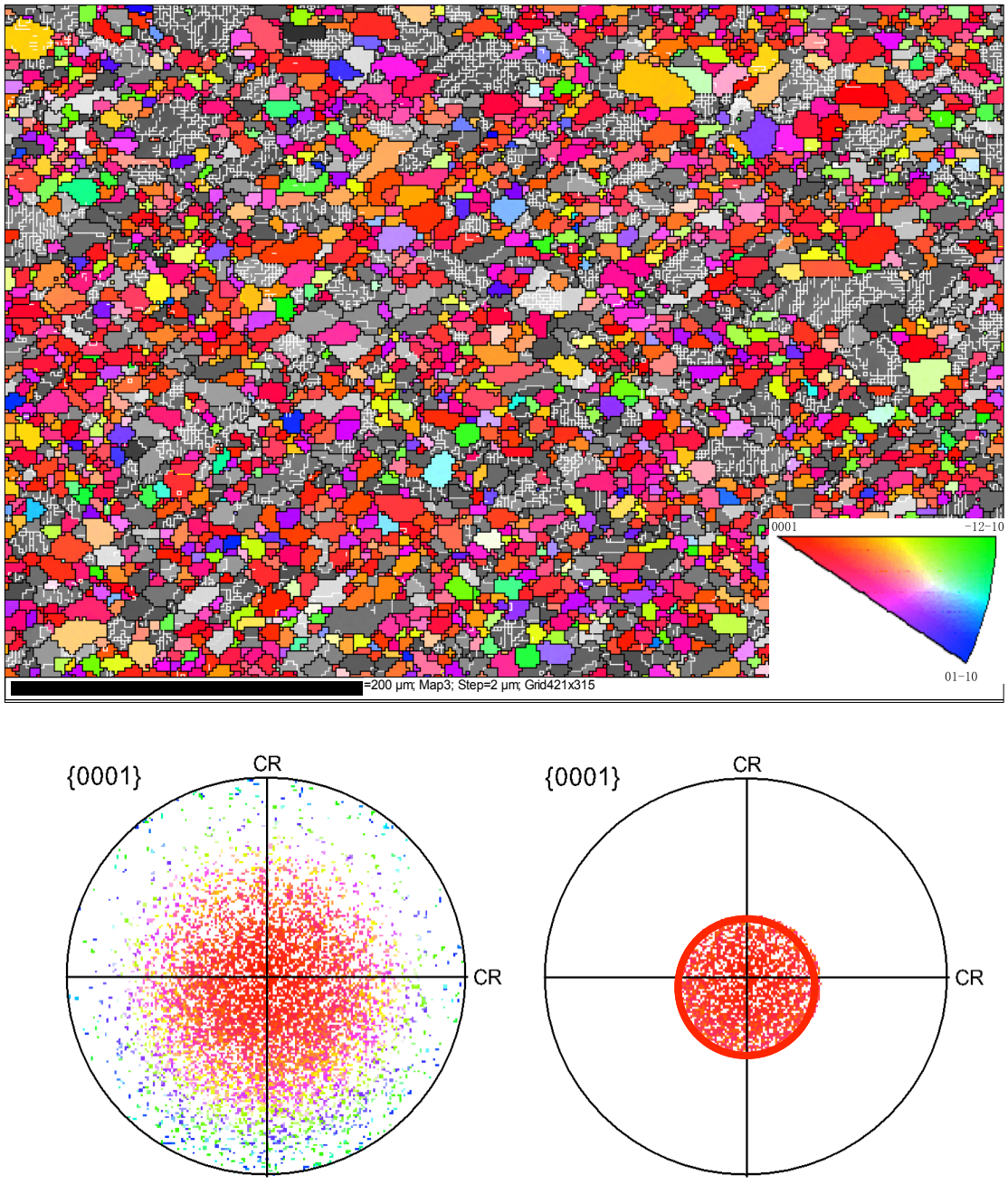

Fig. A4: Recrystallized nuclei orientation analysis of a sample that was 30% deformed and annealed at 250 ^{o}C for 1000s.

Appendix 2

Recrystallization Nucleation Mechanism Discussion

As we discussed earlier, the recovery of magnesium alloy is relatively rapid. Dislocation walls or cell structures would form after recovery (Fig. A5 (a)). In one region, marked **x**, in Fig. A5 (b), polygonal subgrain is observed with few internal dislocations. Such area could act as potential recrystallization site when the subgrain boundary further develops to high angle grain-boundary with increasing annealing time.

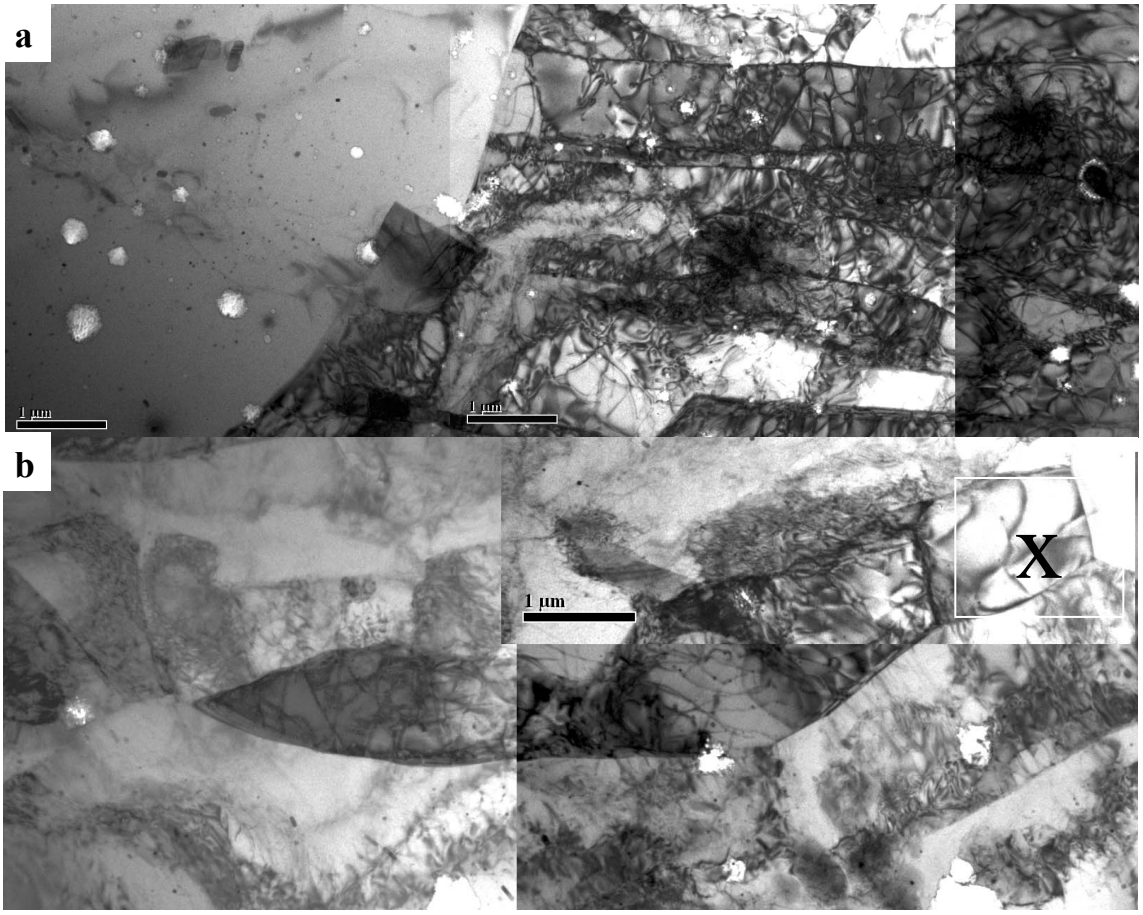

Fig. A5: TEM observations of a sample deformed to the strain of 0.10 and annealed at 250 ^{o}C for 1800s.

The two classical recrystallization nucleation mechanisms are [13]:

- **Strain induced grain boundary migration (SIBM)**: SIBM involves the bulging of part of a pre-existing grain boundary, leaving a dislocation-free region behind the migrating boundary. The characteristic features are that the new grains have similar orientations to the old grains from which they have developed.
- **Subgrain growth within misorientation gradient**: In this model, subgrains formed during annealing grow within a misorientation gradient and gradually build up misorientation until a high angle boundary is formed. The presence of a misorientation gradient is therefore essential for the operation of this mechanism. Humphreys described this nucleation mechanism as discontinuous subgrain growth at sites of high strain energy and orientation gradient, leading to the formation of a high angle boundary that separates low and high strain energy areas.

Under the experimental conditions investigated in this work, SIBM could not be observed except at points where a twin intersects the grain boundary. Fig. A6 is a good example of grain boundary bulging that initiated in the vicinity of a twin-boundary intersection. The second mechanism, i.e. nucleation within a misorientation gradient, was not observed in the low strain specimens. This is consistent with the absence of misorientation gradients at grain boundaries and within twins as confirmed by EBSD observations; misorientation profiles of four different line scans show no significant misorientation gradient in Fig. A7. It should be pointed out, however, that at larger strains,

the necessary misorientation gradient might exist in the highly deformed regions such as shear bands. These areas, however, could not be examined by the EBSD technique.

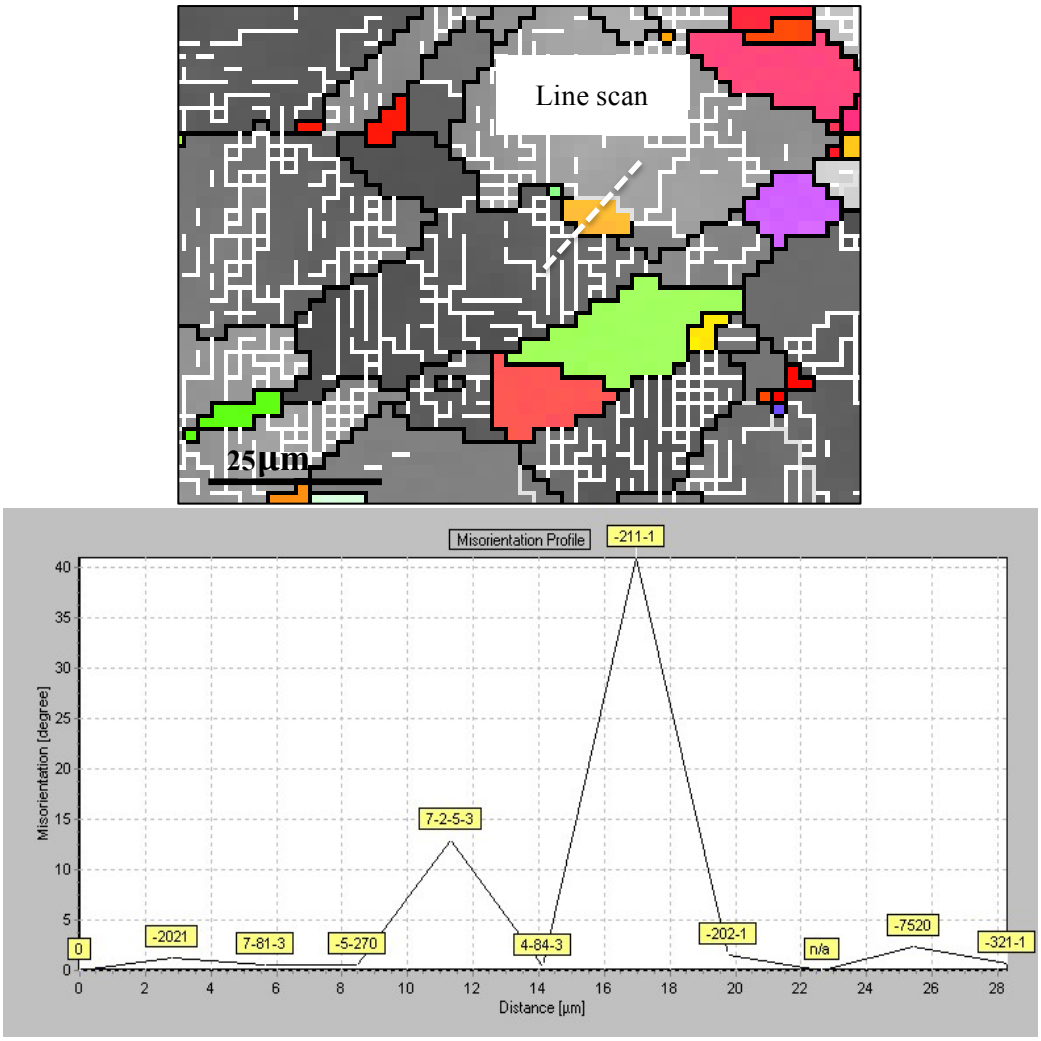

Fig. A6: Recrystallization nucleation of a sample deformed to the strain of 0.10 and annealed at 250 ^{o}C for 1800s.

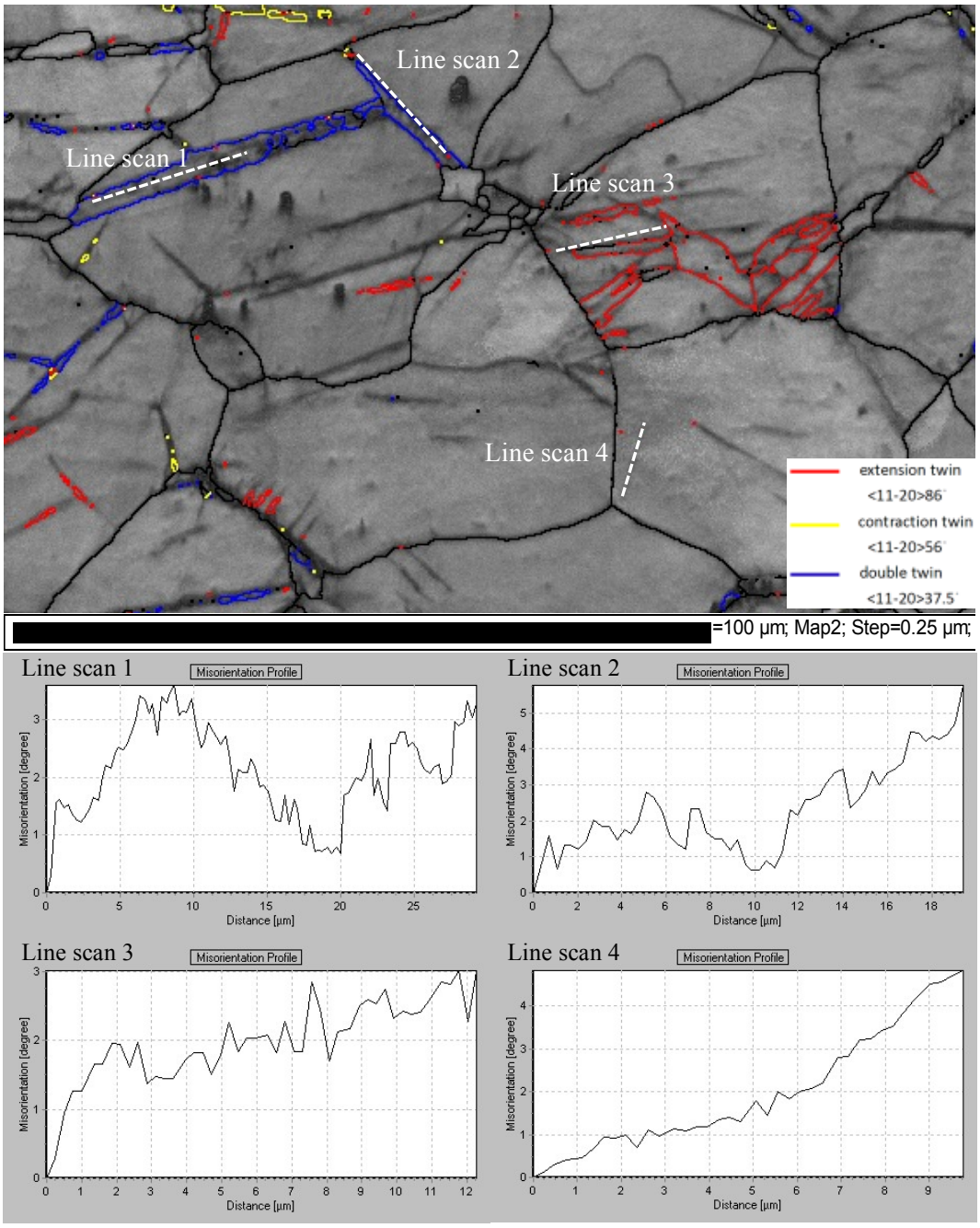

Fig. A7: EBSD band contrast map of a sample deformed to the strain of 0.10. Three types of twins are characterized. Four line scans were conducted within double twins, extension twin and grain-boundary. The misorientation profiles are shown, respectively.

Most of nucleation events that were observed appeared to be associated with twins. Twin/grain-boundary intersections have already been discussed. We also observed nucleation at twin/twin intersections as shown in Fig. 3.8(c). In addition, recrystallization within an individual twin was observed as shown in Fig. 3.4. The mechanism by which this happened is not clear because no misorientation gradients existed within the twin and significant twin boundary bulging was not observed. This leads us to suspect that many of the recrystallization events within twins do not represent recrystallization in the classical sense. It may be more appropriate to describe the appearance of low dislocation density regions in terms of the rapid recovery of the dislocation structure within the twins. This proposition is consistent with the fact that low dislocation regions within the twins typically inherited the elongated twin shape and their misorientation with the matrix continued to be similar to that of the twin-matrix misorientation. This point is illustrated in Fig. A8 where the misorientation was measured for two clusters of "nuclei" within a twin. The misorientation profiles show that the orientations of those nuclei/regions are very close to those of three types of twins (extension twinning (<11-20>86.3^{o}), contraction twinning (<11-20>56.2^{o}) and double twinning (<11-20>37.5^{o})). It seems that these orientation relationships are quite common throughout the whole sample, meaning that most of the "recrystallization nuclei" identified within twins by optical and EBSD methods are in fact recovered regions. This idea is consistent with the observations that low-dislocation density regions within twins do not bulge out into the non-recrystallized matrix.

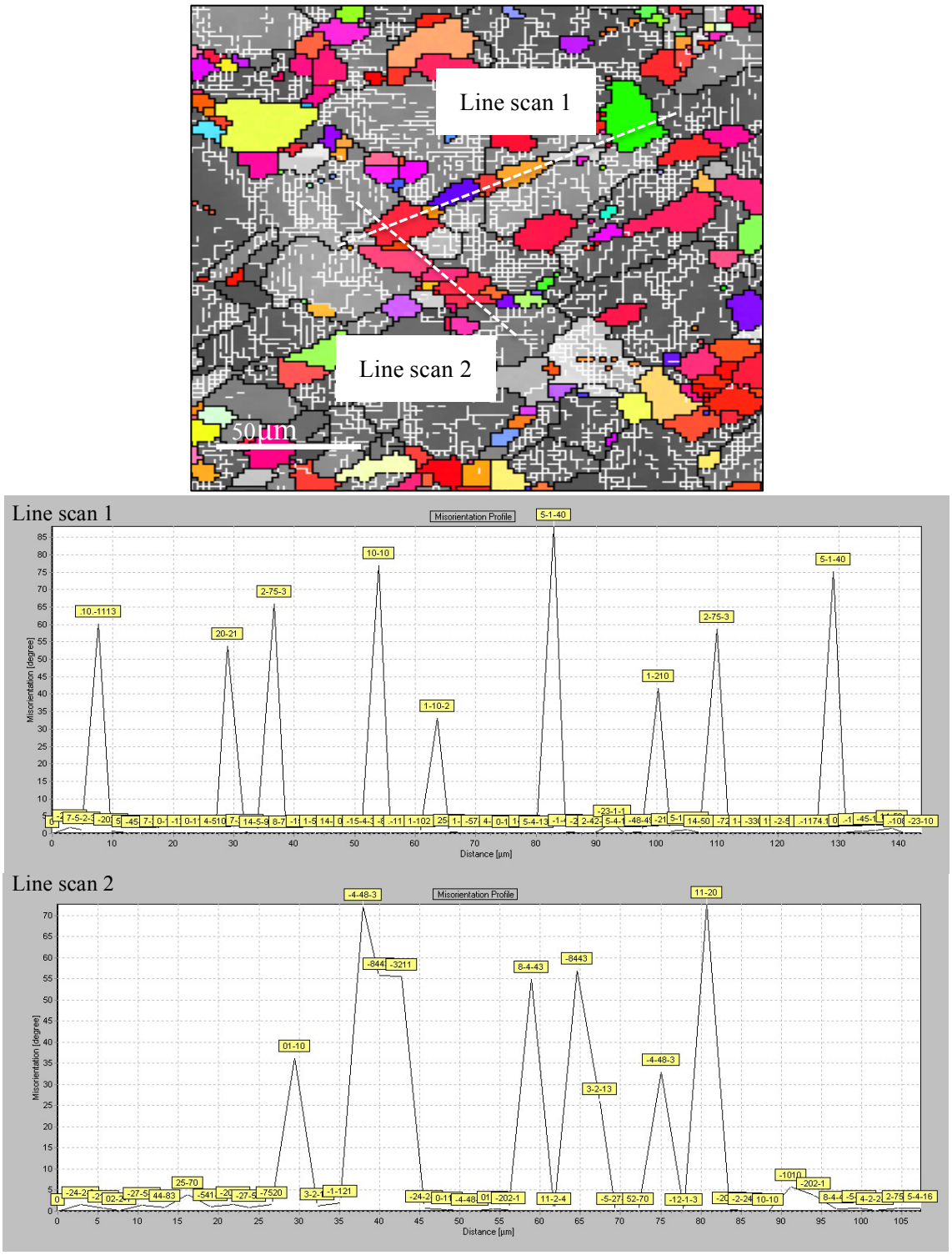

Fig. A8: Recrystallization nucleation of a sample deformed to the strain of 0.10 and annealed at 250 ^{o}C for 1800s.